

**Advanced Nonlinear Optical Waveguides, Switches, Lasers, & Modulators for  
Integrated Intereconnects & Systems**

**FINAL REPORT**

**AUTHORS OF REPORT:** George Stegeman, CREOL, University of Central Florida  
Patrick LiKamWa, CREOL, University of Central Florida  
Ramu Ramaswamy, Dept. of Electrical Engineering,  
University of Florida

**DATES:** 8 September 1991 - March 8, 1995

**U.S. ARMY RESEARCH OFFICE**

**GRANT NUMBER:** DAAL03-91-C-0042

**ARO PROPOSAL NUMBER:** 28996-PH

**UNIVERSITY OF CENTRAL FLORIDA**

**APPROVED FOR PUBLIC RELEASE;**

**DISTRIBUTION UNLIMITED**



19950703 308

DTIC QUALITY INSPECTED 8

The views, opinions, and/or findings contained in this report are those of the authors and should not be construed as an official Department of the Army position, policy, or decision, unless so designated by other documentation.

<b>REPORT DOCUMENTATION PAGE</b>			Form Approved OMB No. 0704-0188	
Public reporting burden for this collection of information is estimated to average 1 hour per response, including the time for reviewing instructions, searching existing data sources, gathering and maintaining the data needed, and completing and reviewing the collection of information. Send comments regarding this burden estimate or any other aspect of this collection of information, including suggestions for reducing this burden, to Washington Headquarters Services, Directorate for Information Operations and Reports, 1215 Jefferson Davis Highway, Suite 1204, Arlington, VA 22202-4302, and to the Office of Management and Budget, Paperwork Reduction Project (0704-0188), Washington, DC 20503.				
1. AGENCY USE ONLY (Leave blank)		2. REPORT DATE June 1995	3. REPORT TYPE AND DATES COVERED Final 6 Sep 91 - 5 Mar 95	
4. TITLE AND SUBTITLE  Advanced Nonlinear Optical Waveguides, Switches, Lasers, & Modulators for Integrated Interconnects & Systems			5. FUNDING NUMBERS  DAAL03-91-C-0042	
6. AUTHOR(S) George Stegeman, Patrick LiKamWa, Ramu Ramaswamy,				
7. PERFORMING ORGANIZATION NAME(S) AND ADDRESS(ES)  University of Central Florida 404000 Central Florida Blvd. Orlando, Florida 32816			8. PERFORMING ORGANIZATION REPORT NUMBER	
9. SPONSORING/MONITORING AGENCY NAME(S) AND ADDRESS(ES)  U.S. Army Research Office P. O. Box 12211 Research Triangle Park, NC 27709-2211			10. SPONSORING/MONITORING AGENCY REPORT NUMBER  ARO 28996.10-PH	
11. SUPPLEMENTARY NOTES The view, opinions and/or findings contained in this report are those of the author(s) and should not be construed as an official Department of the Army position, policy, or decision, unless so designated by other documentation.				
12a. DISTRIBUTION/AVAILABILITY STATEMENT  Approved for public release; distribution unlimited.			12b. DISTRIBUTION CODE	
13. ABSTRACT (Maximum 200 words)  <p style="text-align: center;">This program started in September, 1991 and finished in March 1995, including a no-cost six month extension. There are three independent elements, each with its own principal investigator, namely:</p> <ol style="list-style-type: none"> <li>1. Nonlinear Optical Switching Devices and Circuits - <u>Patrick LiKamWa</u></li> <li>2. Cascading for Third Order Nonlinearities - <u>George Stegeman</u></li> <li>3. Novel Schemes for a Single Quantum Well Laser and Multiquantum Well Waveguide/Modulator Integration - <u>Ramu Ramaswamy</u></li> </ol>				
14. SUBJECT TERMS			15. NUMBER OF PAGES	
			16. PRICE CODE	
17. SECURITY CLASSIFICATION OF REPORT UNCLASSIFIED	18. SECURITY CLASSIFICATION OF THIS PAGE UNCLASSIFIED	19. SECURITY CLASSIFICATION OF ABSTRACT UNCLASSIFIED	20. LIMITATION OF ABSTRACT  UL	

OVERVIEW: This program started in September, 1991 and finished in March 1995, including a no-cost six month extension. There are three independent elements, each with its own principal investigator, namely:

1. Nonlinear Optical Switching Devices and Circuits - Patrick LiKamWa
2. Cascading for Third Order Nonlinearities - George Stegeman
3. Novel Schemes for a Single Quantum Well Laser and Multiquantum Well Waveguide/Modulator Integration - Ramu Ramaswamy

The achievements in each of these programs will be discussed separately.

Accession For		
NTIS	CRA&I	<input checked="" type="checkbox"/>
DTIC	TAB	<input type="checkbox"/>
Unannounced		<input type="checkbox"/>
Justification _____		
By _____		
Distribution /		
Availability Codes		
Dist	Avail and/or Special	
A-1		

## **Final ARO/ARPA report May 1995**

### **Program goals:**

This aim of this project was to explore the feasibility of using a selective area multiple quantum well (MQW) disordering process to achieve monolithic integrated optical circuits made of all-optical switches that operate through bandfilling nonlinearities.

### **Research Achievements:**

#### **Summary of Disordering Concept:**

Optical devices by themselves have limited functional uses. However, used as building blocks to form an integrated circuit, these devices can be potent alternatives to purely electronic devices for processing and routing signals which are already in optical formats such as is the case in telecommunication networks. Various ways of achieving integrated optoelectronic circuits are currently being pursued independently in many research laboratories around the world. Compared to the method of selective etching and re-growth of semiconductors, MQW disordering is a cost effective, simple and highly reproducible technique of achieving different band-gap materials on a single semiconductor substrate. Evidently, this process is only a viable one if MQW material is required for the building block devices. Bandfilling nonlinearities have been demonstrated to be useful in achieving high contrast and low energy all-optical switching devices when MQWs are incorporated into their designs. However, because these devices operate close to resonance with the band-gap, interconnecting them on the same chip requires waveguides with a higher bandgap energy. This is readily accomplished by selective area intermixing. Another consequence of the reliance on the resonant nonlinearity for the switching is that the recovery speed of these devices is directly governed by the rate of removal of free carriers generated for the switching event. Here it was shown that carrier sweep-out in an applied d.c. field can be used to effectively control the recovery rate of these devices to around 100ps time scales.

#### **Executive Summary of Research Achievements:**

1. The hole and electron escape times from a quantum well, have been separately measured in a waveguide containing a single quantum well with symmetric and asymmetric barriers. We have formulated a model that can accurately fit the measured time resolved nonlinear transmission data.
2. The relative importance of the two exciton screening mechanisms has been determined by time resolved spin relaxation measurements.
3. Optical bistability, beam deflection and gain transients in single and multiple quantum well laser diode structures have been measured. We have evidence of strong two-photon absorption from the quantum well barriers and the cladding layers.
4. InGaAs/GaAs MQW self electro-optic effect devices were fabricated and optical bistability has been observed at a wavelength of 980nm with only a 3V external bias in series with a 100kW resistor.



5. SIMS and Auger spectroscopy have been performed on disordered (induced by zinc diffusion) multiple quantum well structures. These confirm the photoluminescence and absorption data on the evolution of the Al intermixing as a function of zinc concentration
6. Rib waveguides have been fabricated in structures that have been intermixed by the diffusion of vacancies that were created by etching off the surface oxides followed by annealing. The waveguide losses have been measured using a thermal Fabry-Perot scanning method. The waveguide losses in the disordered material are on the order of 8dB/cm.
7. An integrated switch consisting of a central dual mode MQW waveguide with disordered input and output branching waveguides has been fabricated and all-optical switching has been demonstrated.

#### Discussion of Research Achievements:

1. Waveguides each containing only a single quantum well with asymmetric barriers i.e. different aluminum concentrations in the AlGaAs barrier layers on either side of the quantum well are used in order to investigate the respective influence of the free electrons and holes on the nonlinear response. Some of this research was carried out in collaboration with AT & T Bell Labs, Holmdel and Amoco Research Labs. These measurements have given individual time constants for electron and hole escape times for different barrier heights as a function of voltage. The measured times are much shorter than those of in an equivalent multiple quantum well device showing that carrier re-trapping is very important in the cross-well transport process. Recovery times down to 10ps have been measured with a d.c. reverse bias field applied to the device. The temperature dependence of the carrier escape times was measured and the results confirm that thermionic emission and drifting are the primary mechanisms by which the carriers leave the quantum well.

We have been fabricating waveguide structures with p and n doping on either side of the waveguide to investigate the effects of lateral sweep-out on the recovery of the nonlinearities in MQW structures. Zn and Ge were selectively diffused into the sample to form the p and n doped regions. These were wire-bonded using silver loaded epoxy to apply external electrical bias across the lateral p-i-n diode thus formed. In our preliminary pump-probe measurements, the transient nonlinear transmission signal has an instantaneous turn-on and the recovery appears to fit with an exponential with a time constant of 500ps. This recovery time constant was reduced to around 200ps with an applied external field. At the present, we are optimizing the fabrication of the doped regions so that a higher electric field can be applied across the waveguide for more efficient carrier sweep-out. Our simple model which uses classical carrier transport by diffusion and drifting to calculate the waveguide overlap integral with the carrier density, predicts a recovery of the nonlinear transmission that is very close to an exponential curve.

2. The spin relaxation times of excitons in MQW structures were measured using circular polarized pump and probe pulses. The characteristic signatures of the pump-probe signal for different pump and probe polarization combinations lead to information about the relative strength of the two primary mechanisms that cause exciton saturation. The results show that

free-carrier screening (Coulombic) cannot be neglected, although it is smaller in magnitude (about 1:2) than the phase space filling mechanism.

3. Intrinsic optical bistability has been observed in an active InGaAs/GaAs waveguide amplifier confirming that the resonant carrier induced nonlinearity in a gain medium can be useful for all-optical switching. The time resolved measurements on the gain transients revealed rapid transmission changes including strong evidence of two-photon absorption. The recovery of the gain was governed by three time constants, namely two-photon absorption recovery, carrier hole-burning and carrier redistribution, and replenishment of carriers from the external circuit. In a similar active broad area active waveguide devices bias close to threshold, a strong beam was used to deflect the direction of a weak beam.
4. InGaAs/GaAs MQW self-electro-optic effect devices were fabricated and optical bistability was measured at a wavelength of 980nm with only 3V external bias in series with a 100kW resistor. These longer wavelength SEED devices could be better optimized to take advantage of diode pumped Nd:YAG lasers as the optical power supply for SEED array processors. Work still needs to be done to optimize the growth of these structures and push the operating wavelength towards 1.06mm and improve the resonant excitonic absorption strength.
5. Initially we had planned to use Zn diffusion to achieve selective area disordering of the multiple quantum wells. However, from our measurements of dynamic secondary ion mass spectroscopy (SIMS) and dynamic Auger spectroscopy coupled with the photoluminescence and transmission characterization and the waveguide loss measurements, we concluded that any appreciable amount of zinc would result in unacceptably high levels of waveguide loss. In our attempts to reduce the zinc concentration needed for intermixing, we found that the process of removing the surface oxide can lead to the creation of surface group III vacancies. When the sample is then carefully annealed, the diffusion of the vacancies causes intermixing of the Ga with the Al atoms in the MQW layer below. This process is impurity free and hence does not suffer from free-carrier absorption losses.
6. Strip-loaded waveguide structures were fabricated in the disordered sample by wet chemical etching and the propagation losses were measured using a non-destructive thermal scanning of the Fabry-Perot resonator formed by the two cleaved facets. Loss measurements as a function of wavelength show uniform attenuation until about 20meV below the band-edge indicating that band-tailing was minimal. The waveguide losses were measured to be around 8dB/cm in these structures.
7. The impurity-free method of achieving selective area intermixing of MQW structures that was developed during this project was used to fabricate an integrated nonlinear directional coupler with disordered branching waveguides. Switching contrast ratios as high as 5:1 has been achieved in such devices and the recovery of the switching event had a time constant on the order of 160ps. It is believed that the vacancies that were unintentionally introduced into the regions that were protected from the disordering assist in the removal of the photo-generated carriers.

## Papers:

1. R. Bambha, D.C. Hutchings, M.J. Snelling, P. Li Kam Wa, A. Miller, A.L. Moretti, R.W. Wickman, K.A. Stair, T.E. Bird, A. Cavailles, D.A.B. Miller, *Excite-Probe Studies of Carrier Escape Dynamics in a Single Quantum Well Waveguide*, Optical and Quantum Electron, Vol 25, ppS965-S971, 1994.
2. C. Thirstrup, P. N. Robson, P. Li Kam Wa, M. A. Pate, C. C. Button, J.S. Roberts, *Electrooptical Modulation in Multiple Quantum Well Hetero nipi Waveguides*, J. Lightwave Tech., 12(3), p425, 1994.
3. S. Shi, P. Li Kam Wa, A. Miller, Mitra Dutta, J. Pamulapati, P. Cooke, *The Controlled Disorder of Quantum Wells Using Surface Oxidation*, J. of Semicond. Sc. & Tech., 9, p1564, 1994.
4. S. Shi, P. Li Kam Wa, A. Miller, J. Pamulapati, P. Cooke, Mitra Dutta, "A Multi-quantum Well Zero-Gap Directional Coupler with Disordered Branching Waveguides", Appl. Phys. Lett., 66(1), p79, 1995.
5. H. S. Wang, P. Li Kam Wa, M. Ghisoni, G. Parry, P. N. Stavrinou, C. Roberts, A. Miller, *Ultrafast Recovery in a Strained InGaAs/AlAs MQW pin Modulator*, Photonics. Tech. Lett., 7(2), p173-175, 1995.

## Contributed Conference Presentations

1. *Integration of a GaAs/AlGaAs All-Optical Switch with Disordered Branching Waveguides*, LEOS'94 Annual meeting, Boston, 1994.
2. *A new technique of quantum well disordering and its application to integrated all-optical switches*, NATO Summer School, Bulgaria, September 19-23 1994.
3. *Strained InGaAs/AlAs MQW pin Modulator with Ultrafast Recovery*, OSA/IEEE Topical meeting on Quantum Optoelectronics, Dana Point California, February 1995.
4. *All-Optical Integrated Devices using Multi-quantum Well Disorder*, SPIE meeting on Aerospace/Defense Sensing and Dual-Use Photonics, Orlando, April 1995.
5. *Ultrafast Recovery and Bistable Switching in Strained InGaAs/GaAs(AlAs) Modulators*, CLEO 95, Baltimore, May 1995.
6. *Selective Area Disorder of Multi-quantum Wells in Integrated Optical Devices*, CLEO 95, Baltimore, May 1995.

functioning as an etched mirror to provide optical feedback for the laser. This increased the threshold current density by a factor of  $\sim 2$ . High coupling losses were present due to the presence of the trench.

4c. A prototype integrated chip was fabricated utilizing N implantation in the tapered interconnect section, and etching a trench between the laser and taper. The modulator performance was equivalent to that of a discrete device.

Scientific Personnel Supported by this project and degrees awarded:

*Faculty:* A. Miller, P. LiKamWa

*Postdoctoral Fellow:* M. Snelling (24months)

*Graduate Students:* X. Shi, H.S. Wang, M. Perozzo

*Ph.Ds Awarded:*

Xinyue (Shawn) Shi (ECE), November 7, 1994.

*The disordering of GaAs/AlGaAs multiple quantum wells and its application in the fabrication of integrated optical devices*

Haisheng Wang (Physics), January 30, 1995.

*Transient electro-optical nonlinearities in strained multiple quantum wells in InGaAs/GaAs (AlAs) pin modulators*

Margaret Perozzo (Physics), March 21, 1995.

*Exciton saturation and spin relaxation in GaAs multiple quantum wells*

## PART 2: CASCADING FOR THIRD ORDER NONLINEARITIES - George Stegeman

**PROGRAM GOALS:** The goal was to demonstrate the cascading of second order nonlinearities to effectively produce third order nonlinearities. The cascading phenomenon was to be studied theoretically and experimentally in order to identify new phenomena and applications.

### RESEARCH ACHIEVEMENTS:

#### Summary of Cascading Concept:

The nonlinear phase shifts associated with third order nonlinearities are used for phase conjugation, all-optical devices, solitons etc. It has been known since the early days of nonlinear optics that second order susceptibilities can lead to effects similar to third order susceptibilities. In fact for a single input wavelength this process requires both up conversion (second harmonic generation) and down conversion (the mixing of the generated second harmonic with the fundamental to produce photons at the fundamental wavelength). This is shown schematically in Fig. 1. The distance which a second harmonic photon travels before returning via down conversion to the fundamental beam is typically the coherence length, making this a non-local process. If the process is not phase-matched, the phase velocities are not equal, i.e.  $v_1 \neq v_2$ , then the photons returning to the fundamental after a propagation distance  $L$  are shifted in phase (relative to the fundamental beam) by  $\Delta\phi \approx \pi - 2[n(\omega) - n(2\omega)]L\omega/c$ . The  $\pi$  serves to conserve energy in this interaction and is a consequence of the nonlinear coupling between the two beams. That is for the phase-matched case where there is no down conversion, the photons returning to the fundamental are  $\pi$  out of the phase with the fundamental which leads directly to pump depletion. The "nonlinear phase shift" associated with this cascading process is given by the index difference term. It is nonlinear because the number of second harmonic photons is proportional to the input fundamental intensity, and hence the induced phase shift is also proportional to the input intensity. This effect can be used for just about any nonlinear optics phenomenon which requires a nonlinear phase change, such as all-optical devices, spatial solitons etc. The goal of this program was to verify this phenomenon experimentally and search for unique applications.

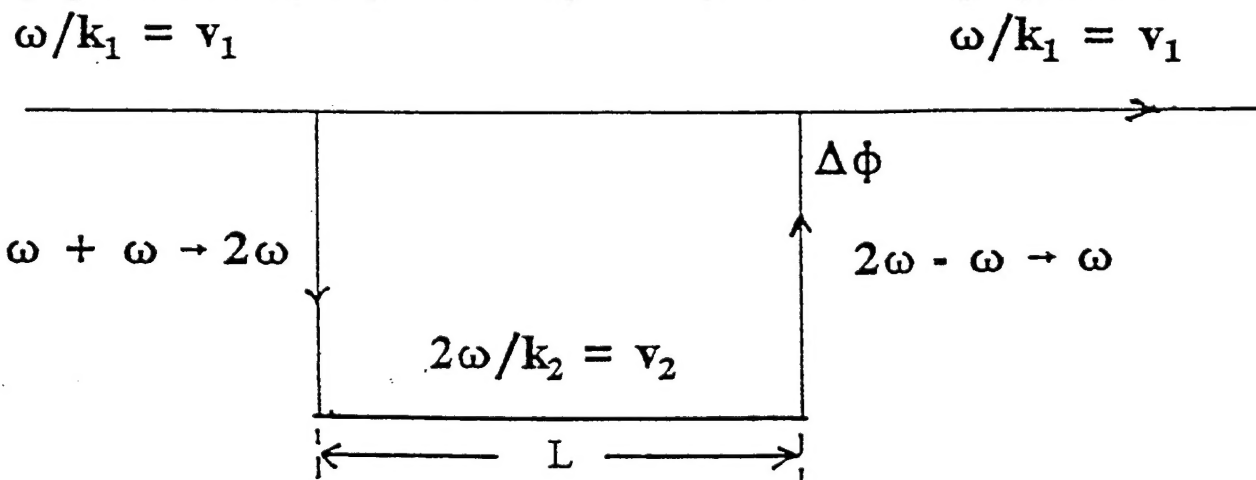


**Fig. 1** Schematic diagram of the cascading process for producing phase shifts.  $L$  is typically the coherence length.

### Executive Summary of Research Achievements:

1. The key features of the cascading nonlinear phase shifts were elucidated by theoretical modelling.
2. Very large cascading phase shifts ( $\rightarrow 2\pi$ ) were demonstrated in KTP waveguides near the phase-matching condition for QPM waveguides.
3. The generation of cascading phase shifts was verified for the Cerenkov second harmonic geometry in organic crystal core fibers.
4. The variation in the nonlinear phase with detuning from the phase-matching condition was measured in apodized LiNbO<sub>3</sub> channel waveguides. Phase changes  $> 1.5\pi$  were measured with minimum conversion of fundamental to second harmonic.
5. A prototype nonlinear Mach-Zehnder all-optical switch was demonstrated.
6. The existence of spatial solitary waves for beams with one- and two-transverse dimensions was predicted and conditions for observation defined.
7. One-dimensional spatial solitons were demonstrated experimentally.
8. Two-dimensional spatial solitary waves were observed and the concept of "soliton locking" of the fundamental and second harmonic waves was discovered.

### Discussion of Research Achievements:

1. Second harmonic generation has been studied theoretically for the lossless near phase-matched case. Many features are different from a standard third order nonlinearity, namely:
  - (i) The nonlinear phase shift produced in the fundamental beam accumulates linearly with distance in maximum steps of  $\pi/2$ , one step for each oscillation in the fundamental power with distance.
  - (ii) The increase in phase is initially linear with power, but for large phase shifts becomes linear in the fundamental amplitude.
  - (iii) Detailed calculations for existing materials (assuming that they can be phase-matched) indicate non-resonant,  $\pi/2$  phase changes are possible for sub-watt input powers.
  - (iv) Large changes in fundamental power and output phase can be achieved by "seeding" the input with a small second harmonic signal.

We have examined whether this unique nonlinear response is useful for all-optical switching devices.

- (i) A nonlinear Mach-Zehnder interferometer, under certain conditions, can show complete switching without the pulse break-up normally associated with  $n_2$ .
- (ii) However, the best response for a nonlinear directional coupler exhibits incomplete switching (similar to that obtained with  $n_2$ ), but with strong modulation of the output pulse.
- (iii) There are three features which make this process interesting for an all-optical transistor. With appropriate inputs, we can control: the output amplitude, the output phase, the net gain.

2. Large nonlinear phase shifts were found in quasi-phase-matched KTP channel waveguides near SHG phase-matching by measuring the spectral broadening as a function of power, and wavelength detuning from the phase-matching condition with a tunable, picosecond Ti:sapphire laser. Just away from phase-matching, the spectrum broadens and splits into multiple peaks with



increasing power, corresponding to a maximum nonlinear phase shift of  $2\pi$ . The variation in the spectral broadening with detuning from phase-matching also agreed with that expected from the cascading process. Right on phase-matching, there is no nonlinear phase shift. The nonlinear phase shift reaches a maximum on both sides of the phase-matching condition, and then decays with increasing detuning from phase-match. We were able to simulate all of the observed spectra by solving the pulsed version of the coupled SHG equations, including phase and group velocity dispersion.

3. Phase shifts of  $\pi/4$  due to Cerenkov SHG was measured in DAN crystal core fibers with only a few percent loss of the fundamental into the second harmonic. In this case, the generated second harmonic is radiated out of the fiber core and the phase shift is caused by the photon exchange between the guided fundamental and the second harmonic multireflected in the core. BPM modelling has shown reasonable agreement with experiment, given that the dispersion of DAN with wavelength is not well-known. NPP core fibers (larger nonlinearities than DAN) have been examined with mixed results, i.e. the nonlinear phase shifts have been small.

4. Effective nonlinearities have been measured in  $\text{LiNbO}_3$  channel waveguides using mode conversion  $[\text{TE}_{00}(\omega) \rightarrow \text{TM}_{00}(2\omega)]$  with Type I phase-matching at  $360^\circ\text{C}$  at 1320 nm. The key was that the temperature profile in the oven (and therefore the wavevector-matching condition) was not uniform with propagation distance and it resulted in nonlinear phase shifts with negligible SHG conversion and a broader bandwidth than expected from constant wavevector mismatch along the full length of the sample. This implies that by apodizing the wavevector matching condition, the SHG conversion (fundamental loss) can be minimized, the bandwidth enhanced and probably the temporal pulse profile controlled.

Experiments have also been performed on quasi-phase-matched  $\text{LiNbO}_3$  channel waveguides. This system was single mode at 1550 nm and multi-mode at 775 nm, the harmonic wavelength. We observed interference effects between two closely-spaced, doubled, guided modes due to the nonlinear phase shift induced at one mode due to the presence of the other, and vice-versa. This has implications to efficient SHG.

5. A prototype, all-optical, hybrid Mach-Zehnder interferometric switch has been demonstrated based on cascading in lithium niobate channel waveguides. The device was hybrid in the sense that the interferometer reference arm was in air.

6. Calculations for modelling the existence of spatial solitons via cascading were performed. The conditions for the excitation of spatial solitons in slab waveguides and in bulk media were defined for real materials, as well as some initial results on stability (more robust than Kerr nonlinearity solitons).

7. Spatial solitons due to cascading have been observed experimentally in  $\text{LiNbO}_3$  slab waveguides. Beams which can diffract in the plane of the waveguide were launched into Type I phase-matched waveguides and the output beam width was measured as a function of input power and wavevector-matching (effective nonlinearity). At low powers the beam diffracted to 4 times its original size. At exactly, the power calculated for spatial soliton formation, the



output beam width equalled the input beam width.

8. Spatial solitary waves were observed in KTP Type II wavevector matched crystals. A new phenomenon called "soliton-locking" has been discovered in which the fundamental and second harmonic are locked together in space, even when "walk-off" is obtained in normal SHG. The output beam width for both the fundamental and harmonic was about 25% less than the input beam widths, independent of input power once a threshold incident intensity is exceeded. (At low powers the output beams increased by a factor of 5 due to diffraction.) Furthermore, the SHG conversion becomes insensitive to exact phase-matching, i.e. the strong coupled fundamental-harmonic interaction causes the interaction to automatically pull itself onto phase-matching. This result suggests a new range of parameters for optimizing parametric interactions for frequency conversion.

## **Publications:**

### **(a) Papers**

1. G.I. Stegeman, M. Sheik-Bahae, E. VanStryland and G. Assanto, "Large nonlinear phase shifts in second order nonlinear optical processes", *Opt. Lett.*, **18**, 13 (1993)
2. G. Assanto, G.I. Stegeman, M. Sheik-Bahae and E. VanStryland, "All-optical guided wave devices based on second order nonlinearities", *Appl. Phys. Lett.*, **62**, 1323 (1993)
3. D.Y. Kim, W.E. Torruellas, J. Kang, C. Bosshard, P. Vidakovic, J. Zyss, W. Moerner, R. Twieg and G. Bjorklund, "Second Order Cascading as the Origin of Large Third Order Effects in Organic Single Crystal Core Fibers" *Opt. Lett.*, **19**, 868 (1994).
4. M.L. Sundheimer, A. Villeneuve, G.I. Stegeman and J.D. Bierlein, "Simultaneous Generation of Red, Green and Blue Light in a Segmented KTP Waveguide Using a Single Source", *Electron. Lett.*, **30**, 975 (1994).
5. L. Torner, C.R. Menyuk and G.I. Stegeman, "Excitation of Soliton-like Waves with Cascaded Nonlinearities", *Opt. Lett.*, **19**, 1615 (1994).
6. D.J. Hagan, M. Sheik-Bahae, Z. Wang, G.I. Stegeman and E.W. VanStryland, "Phase Controlled Transistor Action by Cascading of Second-Order Nonlinearities in KTP", *Opt. Lett.*, **19**, 1305 (1994).
7. M.L. Sundheimer, A. Villeneuve, G.I. Stegeman and J.D. Bierlein, "Cascading Nonlinearities in KTP Waveguides at Communications Wavelengths", *Electron. Lett.*, **30**, 1400 (1994).
8. R. Schiek, M.L. Sundheimer, D.Y. Kim, Y. Baek, G.I. Stegeman, H. Suche and W. Sohler, "Direct Measurement of Cascaded Nonlinearity in Lithium Niobate Channel

Waveguides", Opt. Lett., **19**, 1949 (1994).

9. W.E. Torruellas, R. Schiek, D.Y. Kim, G. Krijnen, G.I. Stegeman, P. Vidakovic and J. Zyss, "Cascading Nonlinearities in an Organic Single Crystal Core Fiber: The Čerenkov Regime", Opt. Comm, **112**, 122 (1994).

10. P. Vidakovic, J. Zyss, D. Kim, W. Torruellas, G. Stegeman, W. E. Moerner, R. Twieg and G. Bjorklund, "Cascading of Second-order Processes in Quadratic Molecular Media at the Origin of Very Large Cubic Effects", Synthetic Metals, **67**, 303 (1994).

11. L. Torner, C.R. Menyuk, W.E. Torruellas and G.I. Stegeman, "Two Dimensional Soliton-like Waves with Second Order Nonlinearities", Opt. Lett., **20**, 13 (1995).

12. G. Assanto, G.I. Stegeman, M. Sheik-Bahae and E. VanStryland, "Coherent Interactions for All-Optical Signal Processing via Quadratic Nonlinearities", IEEE J. Quant. Electron., QE-31, 673 (1995)

13. L. Torner, C.R. Menyuk and G.I. Stegeman, "Solitons with Second-Order Nonlinearities", JOSA B, in press

14. P. Vidakovic, J. Zyss, D. Kim, W. Torruellas and G.I. Stegeman, "Large Effective  $\chi^{(3)}$  by Cascading  $\chi^{(2)}$  in Crystal Cored Fibers", J. Nonlinear Optics, in press

15. G.M. Krijnen, W. Torruellas, G.I. Stegeman, H.J.W.M. Hoekstra and P.V. Lambeck, "Nonlinear Phase Shifts by Cascading in the Čerenkov Regime", chapter in Guided-Wave Optoelectronics: Device Characterization, Analysis, and Design, Proceedings of the 4'th WRI International Conference on Guided Wave Optoelectronics, edited by T. Tamir, H. Bertoni and G. Griffel, (Plenum Press, New York), in press

16. G.I. Stegeman, R. Schiek, G. Krijnen, W. Torruellas, M. Sundheimer, E. VanStryland, C. Menyuk, L. Torner and G. Assanto, "Cascading: Modelling a New Route to Large Optical Nonlinearities and All-Optical Devices", chapter in Guided-Wave Optoelectronics: Device Characterization, Analysis, and Design, Proceedings of the 4'th WRI International Conference on Guided Wave Optoelectronics, edited by T. Tamir, H. Bertoni and G. Griffel, (Plenum Press, New York), in press

17. W.E. Torruellas, Z. Wang, D.J. Hagan, E.W. VanStryland, G.I. Stegeman, L. Torner and C.R. Menyuk, "Observation of Two-Dimensional Spatial Solitary Waves in a Quadratic Medium", Phys. Rev. Lett., in press

18. W.E. Torruellas, D.Y. Kim, M. Jaegger, P. Vidakovic and J. Zyss, "Cascading of Second Order Nonlinearities: Concepts, Materials and Devices", ACS tutorial series, edited by G. Lindsay, (American Chemical Society, Washington, 1994), in press

19. C.G. Trevino-Palacios, G.I. Stegeman, M.P. DeMichelli, P. Baldi, S. Nouth, D.B. Ostrowsky, D. Delacourt and M. Papuchon, "Intensity Dependent Mode Competition in Second Harmonic Generation in Multimode Waveguides", Appl. Phys. Lett., in press
20. R. Schiek, Y. Baek and G.I. Stegeman, "One-Dimensional Spatial Solitons Due to Cascaded Second-Order Nonlinearities in Planar Waveguides", Phys. Rev. Lett., under revision
21. L. Torner, W.E. Torruellas and G.I. Stegeman, "Beam steering by  $\chi^{(2)}$  trapping, Opt. Lett., submitted
22. D.-M. Baboiu, G.I. Stegeman and L. Torner, "Collision of solitary waves in quadratic media", Opt. Lett., submitted
23. Y. Baek, R. Schiek and G.I. Stegeman, "All-optical response of a hybrid Mach-Zehnder interferometer due to the cascaded nonlinearity", Opt. Lett., submitted
24. W.E. Torruellas, W. Wang, L. Torner and G.I. Stegeman, "Observation of mutual trapping and dragging of two-dimensional spatial solitary waves in a quadratic medium", Opt. Lett., submitted

**(b) Contributed Conference Presentations**

1. "Large Effective Nonlinearities Via Cascading in Organic Fibers", postdeadline paper, ICONO'1, Val Thorens (France), January 1994
2. "Second Order Cascading as the Origin of Large Third Order Effects in Organic Single Crystal Core Fibers", IQEC'94, Anaheim, 1994
3. "Two Dimensional Solitary Waves in a Quadratic Medium: The Experiment", QELS '95, Baltimore, MD, 1995.
4. "Two Dimensional Spatial Solitons with Second-Order Nonlinearities", QELS '95, Baltimore, MD, 1995.
5. "Spatial Solitons Caused by Cascaded Second-Order Nonlinearity in  $\text{LiNbO}_3$  Planar Waveguide", QELS '95, Baltimore, MD, 1995.
6. "Interaction Between Solitons with Second-Order Nonlinearities", QELS '95, Baltimore, MD, 1995.
7. "Cascaded Nonlinearity in Lithium Niobate Waveguides", CLEO '95, Baltimore, MD, 1995.
8. "Intensity Dependent Mode Competition in Second Harmonic Generation in Multimode

Waveguides", CLEO '95, Baltimore, MD, 1995.

9. "High contrast all-optical switching by using cascading in the Čerenkov regime", CLEO '95, Baltimore, MD, 1995.

10. "All-Optical Hybrid Mach Zehnder Switch Due to the Cascaded Second-Order Nonlinearity", CLEO '95, Baltimore, MD, 1995.

11. "Optical Power Limiting by SHG in the Čerenkov Regime", NLGW, Dana Point, CA, 1995.

### **(c) Invited Conference Presentations**

1. "Very large third order nonlinearities via cascading of second order nonlinearities", upgrade from submitted to invited paper, IQEC'92, Vienna, June 1992

2. "Cascading of  $\chi^{(2)}$  for  $\chi^{(3)}$  nonlinearities", Nonlinear Optics: Materials, Fundamentals and Applications, Maui, August 1992

3. "Large nonlinear phase shifts via second order processes", Workshop on "Materials and Devices for ultrafast all-optical switching", Twente, Holland, October 1992

4. "Current Status of Nonlinear Materials and Their Applications to Waveguide Devices", plenary paper at Integrated Photonics Research, Palm Springs, March 1993

5. "Large Nonlinear Phase Modulation in Quasi-Phase-Matched KTP Waveguides due to Cascaded Second Order Processes", upgrade from submitted to invited paper, Nonlinear Guided Wave Phenomena Topical Meeting, Cambridge, September 1993

6. "Perspectives on Third Order Nonlinear Materials for Devices", MITI Conference on Nonlinear Photonics Materials, Tohoku University Japan, May 1994

7. "Cascading of Second Order Nonlinearities: Concepts, Materials and Devices", ACS/OSA Topical Meeting on Organic Thin Films, Washington, August 1994

8. "Large Nonlinear Phase Shifts in Waveguides Due to Cascading of Second Order Nonlinearities", OSA Annual Meeting, Dallas, October 1994

9. "Cascading: A New Approach To All-Optical Phenomena", Symposium on Guided Wave Optoelectronics: Device Characterization, Analysis and Design", Brooklyn, October 1994

10. "Cascading of 2nd Order Nonlinear Processes", European Conference on Integrated Optics, Delft Holland, April 1995

11. "Cascaded Nonlinearity in  $\text{LiNbO}_3$  Waveguides", CLEO'95, Baltimore, May 1995
12. "Cascading: A New Approach to Nonlinear Guided Wave Phenomena", Italian Summer School, Cetaro Italy, May 1995

SCIENTIFIC PERSONNEL SUPPORTED BY THIS PROJECT AND DEGREES AWARDED:

*Faculty:* G.I. Stegeman

*Postdoctoral Fellows:* D. Neher (9 months), C. Bosshard (12 months), W. Torruellas (18 months)

*Graduate Students:* M. Sundheimer, M. Jaegger, Y. Baek, D. Kim

*PhDs Awarded:*

Michael Sundheimer, "Cascaded Second-Order Nonlinearities in Waveguides", PhD Thesis, Fall Semester, completed.

Dug Young Kim, "Interferometric Measurements of Nonlinear Optical Properties for All Optical Switching Applications in Dielectric Waveguides" PhD Thesis, Fall Semester, completed.

REPORT OF INVENTIONS: "Applications of Solitary-Wave Locking in Second Order Parametric Processes", patent applied for

**ADVANCED NONLINEAR OPTICAL  
WAVEGUIDES, SWITCHES, LASERS AND  
MODULATORS FOR INTEGRATED  
INTERCONNECTS AND SYSTEMS**

**CONTRACT NO. DAL 03-91-C-0042  
FINAL REPORT**

**SUBMITTED TO  
UNIVERSITY OF CENTRAL FLORIDA/ARO/ARPA**

**b y**

**R.V.RAMASWAMY  
PHOTONICS RESEARCH LABORATORY  
DEPARTMENT OF ELECTRICAL ENGINEERING  
UNIVERSITY OF FLORIDA  
GAINESVILLE, FL-32611**

## **Executive Summary of Accomplishments:**

### **1. Laser**

- 1a. Asymmetric Fabry-Perot lasers having an equivalent alloy in place of the MQW region were fabricated and had a low threshold current density, inspite of having an extremely small confinement factor  $\Gamma \sim 0.005$ .
- 1b. Fabry-Perot lasers were fabricated from the monolithic structures having an MQW region embedded in the upper cladding after partial disordering of the MQW by Zn implantation, annealing and Zn diffusion.
- 1c. Lasers were fabricated from the monolithic structure, having one cleaved mirror and one etched mirror, with threshold current densities twice the previous case.
- 1d. A novel scheme for high precision p-type Zn doping of the GaAs/AlGaAs structures was developed, which exploits the high vapor pressure of molten Zn at atmospheric pressure.

### **2. Tapered Interconnect**

- 2a. Zn, F, O and N impurity atoms were investigated for impurity induced layer disordering of the MQW's in a tapered geometry, to achieve the three fold target of high refractive index change, low propagation loss and good electrical isolation. Nitrogen was found to be an excellent candidate.
- 2b. A knowledge of the value of  $\Delta n$  is extremely important in refractive index engineering of QW structures for integration purposes. A procedure was developed which utilized Mach-Zehnder measurements, energy level calculations via a variational method for disordered QW's and Photoluminescence spectra of disordered QW's to extract the value of  $\Delta n$  directly from PL shifts, independent of the source or origin of the disordering.
- 2c. Modeling, analysis and numerical optimization of the tapered waveguide structure was done. A new adiabatically invariant structure evolved having complete power transfer from the SQW section to the MQW section.

### **3. Modulator**

Modulators were fabricated from both structures A and B, having on / off ratios of better than 20 dB at 0.85  $\mu\text{m}$  and at low reverse bias voltages (  $< 5 \text{ V}$  ).

### **4. Integration**

- 4a. Integrated tapered waveguide interconnect and modulators were fabricated. Zn diffused taper-modulator integration in structure A had poorer performance than N implanted taper-modulator integration in structure B. The later had an on/off ratio of about 24 dB with a propagation loss of  $\sim 3 \text{ dB/cm}$  in the taper section.
- 4b. Laser-taper integration was completed after developing a scheme to etch a resonator trench of width 5  $\mu\text{m}$  between the laser section and the taper, with one end of the trench

Introduction .....	1
Growth .....	4
LASER .....	7
Asymmetric Laser .....	7
Zinc Diffusion .....	8
MQW Cladding Laser .....	14
Tapered Waveguide Interconnect .....	17
Impurity Induced Layer Disorderng .....	17
Propagation Loss Measurement .....	23
Refractive Index change due to Zn IILD .....	23
Origin of $\Delta N$ in disordered MQW of monolithic structure .....	32
Modeling and Analysis of Tapered Waveguide Interconnect .....	34
Optimization of the Taper Modal Evolution .....	40
MQW Modulator .....	46
Integration of tapered interconnect and modulator .....	54
Integration of Laser-Taper and Modulator .....	62
Summary .....	66
References .....	67
List of Publications .....	68



### **Introduction:**

A key element in future long haul multi-giga-bit optical fiber communication systems and optical computers is a high speed light source. Optical communication systems in the 1.55 micron range require a narrow spectral width for sources under high speed modulation to reduce the effects of chromatic dispersion in single mode fibers. Wavelength chirping or linewidth broadening usually occurs in high speed direct modulation of dynamic single mode lasers such as distributed feedback (DFB) or distributed Bragg reflector (DBR) lasers, and brings about a dispersion penalty in the fiber.

One method to overcome this problem is to use an external modulator. Among the several types of semiconductor modulators which can be integrated with semiconductor lasers, electroabsorption (EA) modulators utilising the Franz-Keldysh effect are attracting attention because of their low driving voltage [1-5], high speed operation [6], and narrow dynamic linewidth [1,7,8].

There have been numerous reports on the monolithic integration of semiconductor lasers and modulator, utilizing an intracavity modulator design and an external modulator design [9-13]. In this study we report on a novel integration design in a monolithic structure composed of a single quantum well (SQW) region and a multi quantum well (MQW) region where the power output from the SQW laser section is transferred to the MQW modulator section via a tapered modal interconnect. It also has a processing advantage in the sense that no regrowth is required after the monolithic structure is grown.

The study reported here is intended to be more of " proof of the principle or concept " and has been done in the Gallium Arsenide/Aluminium Gallium Arsenide ( $\text{GaAs}/\text{Al}_x\text{Ga}_{(1-x)}\text{As}$ ) III-V system. The wavelength region of interest in this system is centered around 0.85 microns.

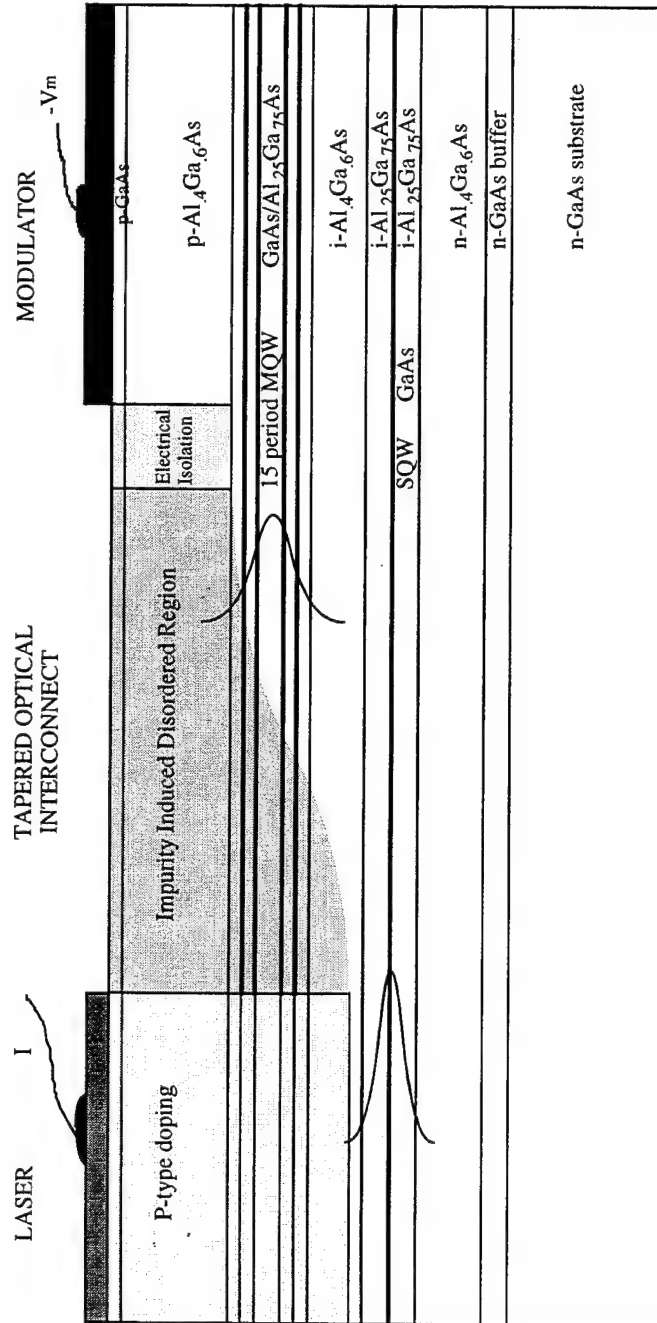


Figure 1: Proposed Integrated Structure

250 Å	GaAs	undoped
5000 Å	Al <sub>40</sub> Ga <sub>60</sub> As	undoped
1000 Å	Al <sub>25</sub> Ga <sub>75</sub> As	undoped
(190 Å (65 Å GaAs Wells) x 15 MQW region undoped	Al <sub>40</sub> Ga <sub>60</sub> As	Barriers) x 14
7000 Å	Al <sub>25</sub> Ga <sub>75</sub> As	undoped
90Å	Single Quantum Well	undoped
2000 Å	Al <sub>25</sub> Ga <sub>75</sub> As	undoped
15,000 Å	Al <sub>40</sub> Ga <sub>60</sub> As	doped n-type 1 e <sup>18</sup>
5000 Å	GaAs	doped n-type 2 e <sup>18</sup>
n <sup>+</sup>	GaAs	substrate

Figure 2a: Structure A

250 Å	GaAs	undoped
7000 Å	Al <sub>35</sub> Ga <sub>65</sub> As	undoped
(190 Å (65 Å GaAs Wells) x 12 MQW region undoped	Al <sub>40</sub> Ga <sub>60</sub> As	Barriers) x 13
5000 Å	Al <sub>35</sub> Ga <sub>65</sub> As	undoped
1500 Å	Al <sub>20</sub> Ga <sub>80</sub> As	undoped
90Å	Single Quantum Well	undoped
1500 Å	Al <sub>20</sub> Ga <sub>80</sub> As	undoped
15,000 Å	Al <sub>35</sub> Ga <sub>65</sub> As	doped n-type 1 e <sup>18</sup>
5000 Å	GaAs	doped n-type 2 e <sup>18</sup>
n <sup>+</sup>	GaAs	substrate

Figure 2b: Structure B

This report is divided into five sections dealing with the laser, tapered modal interconnect, modulator, integrated modulator and modal interconnect, and the total integration, respectively. Figure 1 shows in schematic the lateral cross-section of the conceptual integrated structure.

Two types of monolithic structures were studied as illustrated in figure 2. In structure A, the design is unoptimized with respect to modal evolution of power in the taper. We report on Zinc (Zn) and Fluorine (F) impurity induced disordering, propagation loss measurements, refractive index change, modeling of near field profiles of the taper, a modulator, and an integrated taper-modulator formed via Zinc diffusion in this structure. In structure B, the design is optimized with respect to the modal evolution of power in the taper. We report on the numerical optimization of the taper, Oxygen (O) and Nitrogen (N) impurity induced layer disordering, propagation loss measurements, integrated taper modulator, laser-taper and modulator integration utilizing Zinc and Nitrogen implantation.

### **Growth:**

All epitaxial growth was performed in an atmospheric pressure metalorganic chemical vapor deposition (MOCVD) system at a temperature of 725 °C using Tri-Methyl Aluminum (TMA), Tri-Methyl Gallium (TMG), and Arsine ( $\text{AsH}_3$ ) as the precursors. The growth rate used was 300 Å per minute with a V/III mole ratio of 40. GaAs wafers of (100) orientation, doped n-type with a doping density of  $1 \times 10^{18}/\text{cm}^3$  were used as substrates.

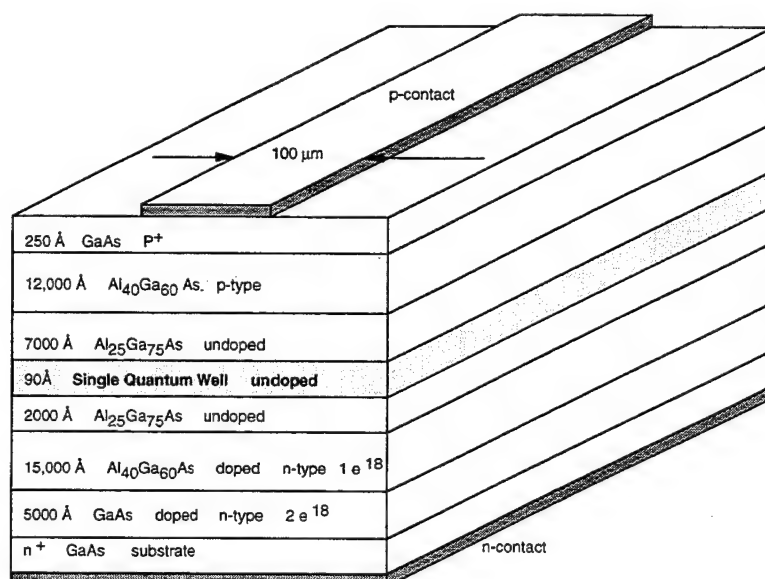


Figure 3: Schematic of broad-area asymmetric SQW laser

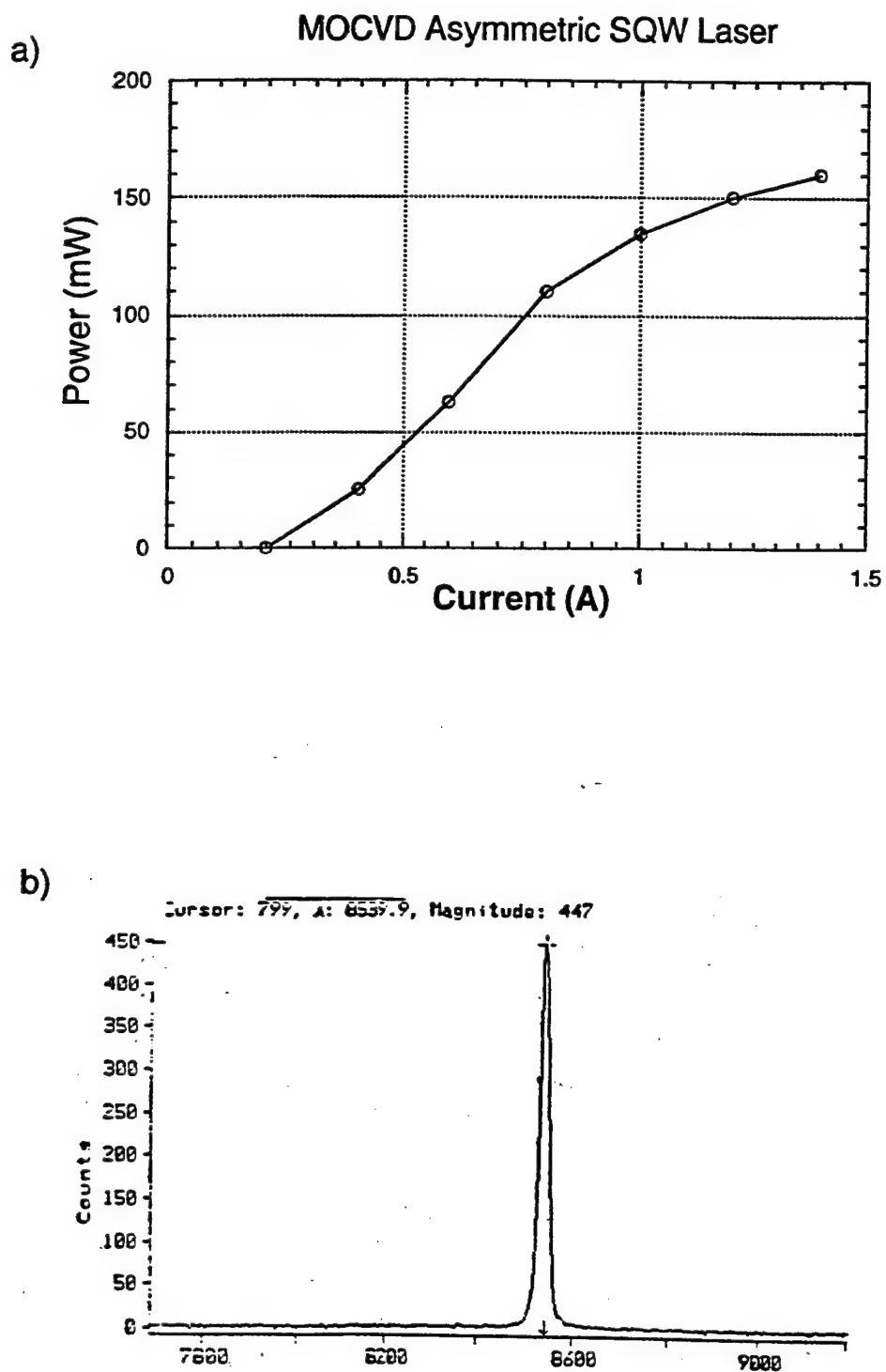


FIGURE 4: Lasing characteristics of the broad-area asymmetric SQW laser in Fig.3. a) power versus injection current , b) lasing spectrum

## LASER:

### Asymmetric Laser:

As shown in figure 1 of the introduction, the proposed laser- modulator integrated device has an asymmetric waveguide due to the presence of the MQW in the upper cladding in the laser section. Due to relatively poorer light confinement caused by the asymmetry an increase in the threshold current density is expected. To test this hypothesis we grew an asymmetric SQW structure with part of the upper cladding and the MQW region replaced by a 0.7 micron thick  $\text{Al}_{25}\text{Ga}_{75}\text{As}$  layer. Broad area lasers were fabricated by evaporating 100 micron wide Ti/Au stripes on the top surface for p-type contacts, and Au-Ge on the bottom surface for n-type contacts after lapping down the substrate side to 100 microns. The samples were then cleaved into lengths of 500 microns. Figure 3 is a schematic of this broad area asymmetric laser.

Figure 4a shows the measured light output power versus injection current under pulsed operations with a 1 micro-second pulse width and 2 KHz repetition rate. A calibrated Si photodiode was used to detect the optical power. The threshold current is 300 mA, corresponding to a threshold current density of about  $600 \text{ A/cm}^2$ . This threshold current density is a factor of about two times larger than the lowest threshold current densities reported for GaAs/AlGaAs graded index waveguide separate confinement heterostructure (GRINCH) SQW lasers. However, we must realize that these asymmetric SQW lasers are relatively very efficient as they lase with a reasonably low threshold current density in spite of an extremely small confinement factor  $\Gamma$  of less than 0.005 compared to confinement factors of  $\sim 0.03$  for symmetric GRINCH SQW lasers. Figure 4b shows the measured spectrum of the laser. It peaks at  $\lambda = 0.854$  microns with a full width at half maximum (FWHM) of  $\sim 20 \text{ \AA}$ , which is a typical value for broad area GaAs/AlGaAs SQW lasers. These results show that asymmetric SQW lasers with their good lasing characteristics are indeed quite suitable for SQW laser-MQW modulator integration.

In the monolithic structure B, the active region of this asymmetric laser is a 90 Å GaAs single quantum well, surrounded by 1500 Å Al<sub>20</sub>Ga<sub>80</sub>As barriers. The lower cladding is 1.5 microns of an Al<sub>35</sub>Ga<sub>65</sub>As alloy doped n-type to a carrier concentration of 1.0e18. The upper cladding has embedded in it an MQW region consisting of 13.5 pairs of 190 Å Al<sub>40</sub>Ga<sub>60</sub>As barrier and 65 Å GaAs well. In addition the upper cladding is undoped.

It is clear however, that for the structure to function as a laser, proper p-type doping of the upper cladding would be required. With this in mind a novel Zn vapor diffusion scheme for precision p-type doping was developed.

### **Zinc Diffusion:**

Post-growth diffusion of Zn into III-V semiconductor device structures is of paramount importance for p-type doping and ohmic contacts e.g., semiconductor lasers. For other opto-electronic devices, often, it is useful in bandgap and refractive index engineering of multi quantum well and superlattice structures that utilize Zn impurity induced layer disordering. However, the majority of post growth Zn diffusion schemes utilize the sealed ampule technique with Zinc Arsenide compounds as the Zn source. The samples are usually capped to prevent Arsenic (As) out diffusion, and with diffusion temperatures around ~800 °C and diffusion times of the order of an hour.

Here, we exploit the high vapor pressure of molten Zn, at atmospheric pressure, for Zn diffusion into these GaAs/AlGaAs structures, with meaningful diffusion carried out at 600 °C and 700 °C for times less than 15 minutes, resulting in high Zn surface concentrations along with deep diffusion and good activation. The process is highly reproducible. This technique utilized a two tier graphite cell with metallic Zn at the lower level and the sample at a higher level. This cell was kept inside an unsealed, capped quartz crucible which in turn was placed inside an LPE furnace tube with flowing nitrogen gas. This tube is then inserted into the hot furnace and our diffusion clock was



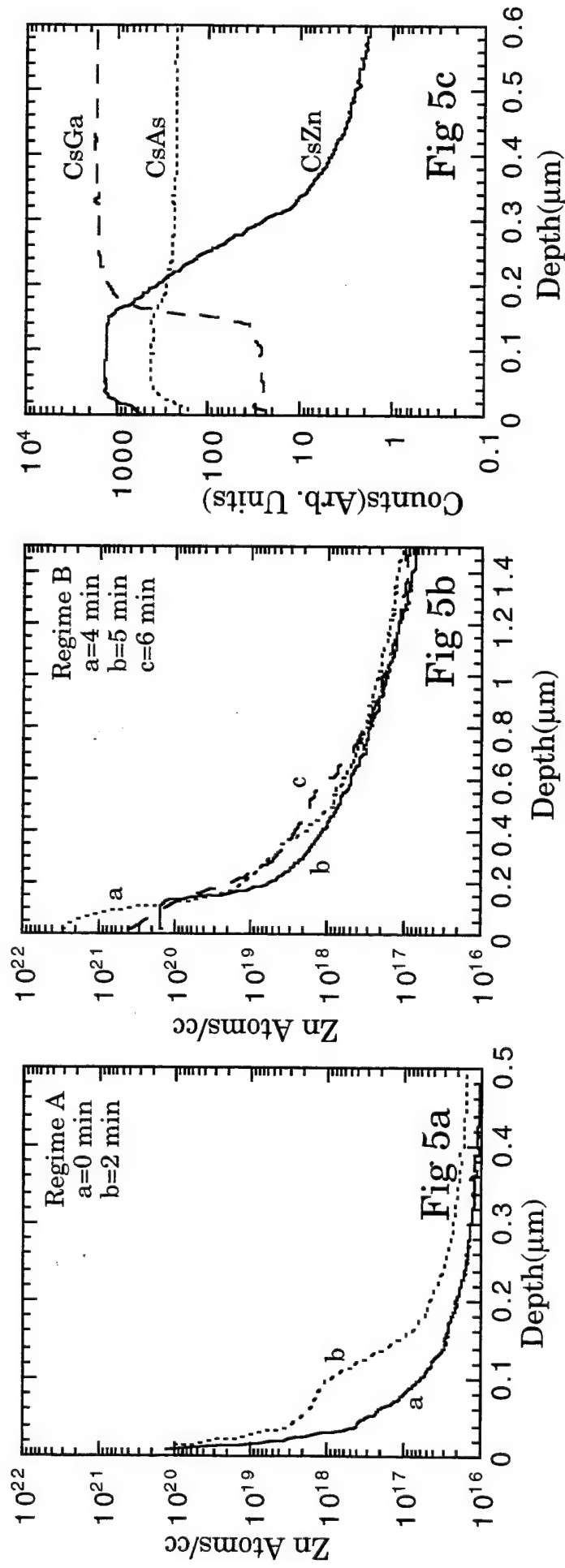


Figure 5a,b: Zinc profiles under time evolution for different time regimes  
 Figure 5c : Zn, Ga and As profiles at surface for 5 minutes

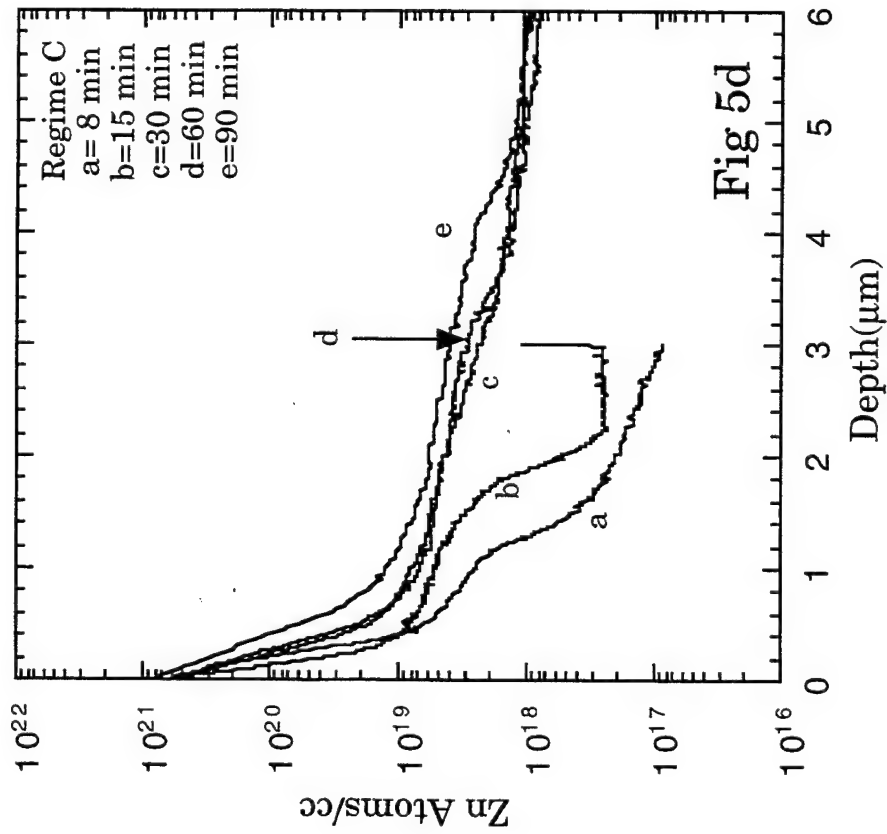


Figure 5d: Zn profiles for large time scales

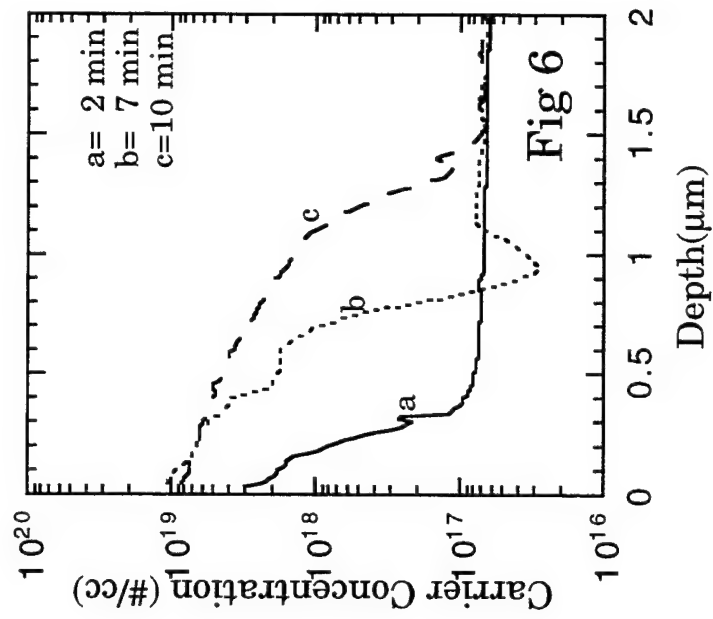


Figure 6: p-type carrier concentration profiles

started when the cell temperature reached the desired temperature. All of the samples showed no surface damage after diffusion and exhibited a mirror finish.

The time evolution of the SIMS Zn diffusion profiles in semi-insulating GaAs are shown in figures 5a through 5d and can be separated into three time regimes; A, B, C where the time scales are  $0 < A < 4$ ;  $4 < B < 6$ ; and  $6 < C < \infty$ , in minutes. These diffusions were done at  $600^{\circ}\text{C}$

In regime A (figure 5a), shoulders are observed in the profiles. The shoulders occurs at higher concentrations and deeper in the crystal with increasing time, i.e., at 0.05 and 0.1 microns for 0 and 2 minutes respectively. These profiles are consistent with the Frank-Turnbull substitutional-interstitial equilibrium mechanism which involves Zn being present both as an interstitial and substitutional species.

In regime B (figure 5b) the shoulder starts to vanish and the surface concentration of Zn rises rapidly at about 4 minutes. A chemical reaction is then triggered off to form a Zn-Ga-As alloy. This can be seen in figure 5c, as a constant value of Zn for about 0.15 microns in the SIMS profile for 5 minutes. The color of the sample also changed to a metallic golden brown. Then at about 6 minutes the diffusion profile changes again, with the constant value at the surface vanishing. Another point of interest is that the concentration profiles in the regions deeper than 0.5 microns are similar for all times.

In regime C (figure 5d), for times greater than 6 minutes, deep diffusion begins to occur. All these profiles have three different regions: an initial profile which becomes increasingly linear with longer diffusion times, a mid section resembling a shoulder and a deep tail region of lower Zn concentration.

Technically, the important time scales for diffusion in this scheme are a few minutes for contacts and less than  $\sim 15$  minutes for deep diffusion, where useful substitutional diffusion occurs to a depth of about 2 microns, for temperatures less than  $700^{\circ}\text{C}$ .

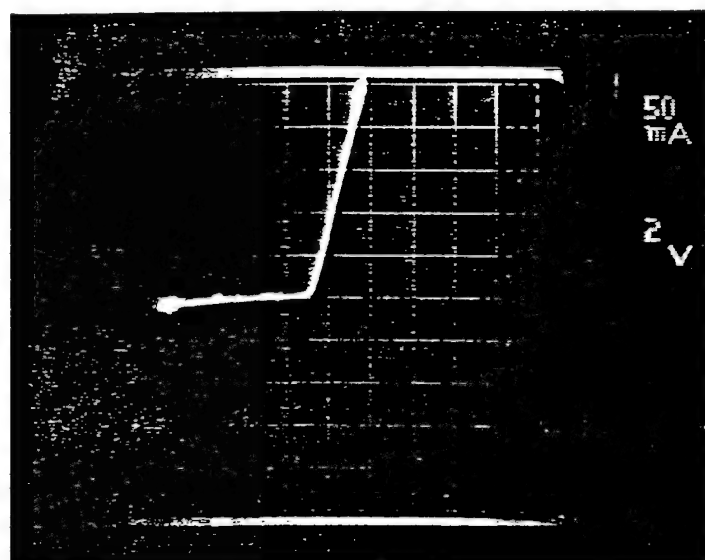


Figure 7: I-V curve for sample of structure B , Zn diffused for 2 minutes

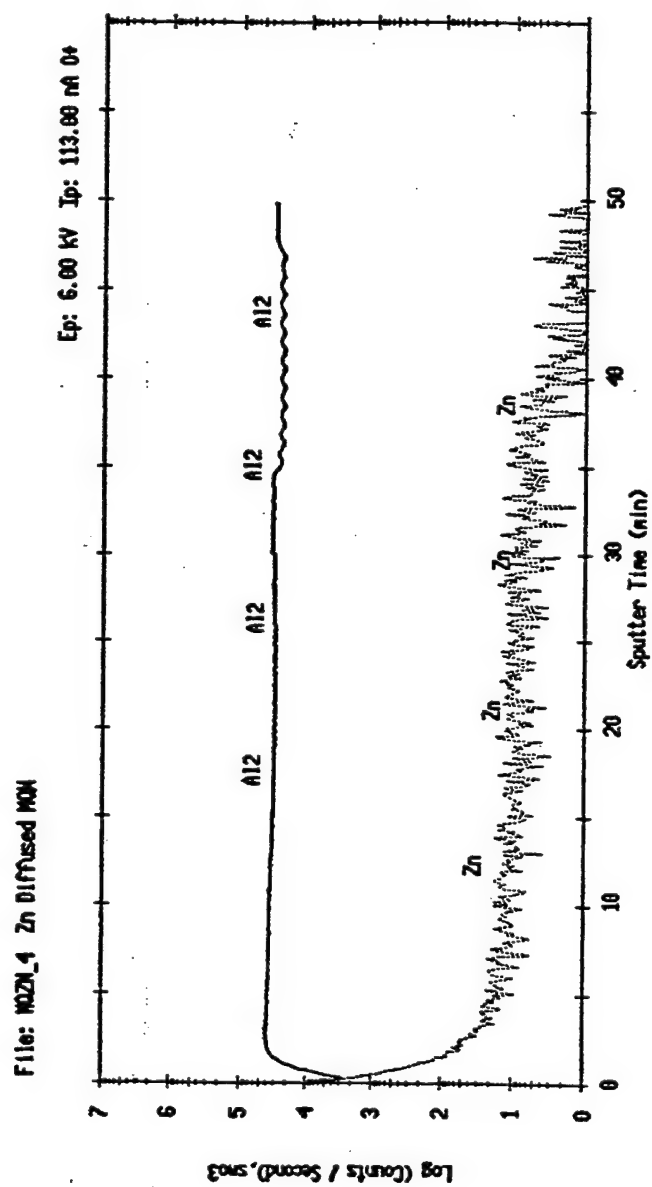


Figure 8: SIMS AL and Zn profiles for sample Zn diffused for 2 minutes

Figure 6 shows the carrier concentration profiles for three different diffusion times, done at  $600^{\circ}\text{C}$ , into n-type (doping density  $7.5 \times 10^{17}/\text{cm}^3$ ) GaAs as obtained by electro-chemical profiling. Useful carrier concentrations are obtained within 10 minutes. However, for the 5 minute diffusion no liquid Schottky diode could be formed. The I-V characteristics showed low resistance ohmic contacts and the rest potential indicated p-type material. This further implied that a p-type Zn-Ga-As alloy was formed on the surface.

#### **MQW Cladding Laser:**

As grown samples of monolithic structure B, of  $0.5 \times 0.5 \text{ cm}^2$  area were then diffused with Zn at a temperature of  $700^{\circ}\text{C}$  for various times. The best I-V curves were obtained for 2 minutes diffusion as shown in figure 7. However, the samples behaved as light emitting diodes (LEDs) without any laser action.

SIMS profiles of Al and Zn shown in figure 8 in the two minutes diffused, samples showed that though Zn had diffused to the correct depth and concentration, the embedded MQW was still intact.

An analysis of the monolithic structure indicated that the MQW section is equivalent to an alloy of composition close to  $\text{Al}_{0.05}\text{Ga}_{0.95}\text{As}$  and hence has a refractive index close to that of bulk GaAs. Such a layer of 0.4 microns thickness, embedded in the cladding and 0.5 microns away from the SQW would shift the transmission resonance of the Fabry-Perot structure away from the SQW transition of 0.85 microns, and hence no laser action would be observed. A way to get around this problem would be to intermix the MQW completely, to give an equivalent alloy of about  $\text{Al}_{27}\text{Ga}_{63}\text{As}$  having a refractive index close to the rest of the cladding.

With this in mind, a systematic study of the MQW disordering via Zn implantation and subsequent annealing was undertaken. Laser action was obtained when the Zn implant energy was  $> 150 \text{ KV}$  with a dosage of  $1.0 \times 10^{15} \text{ ions}/\text{cm}^2$ . A maximum energy of 170 KV was obtainable due to instrument constraints. A 2 minute Zn diffusion

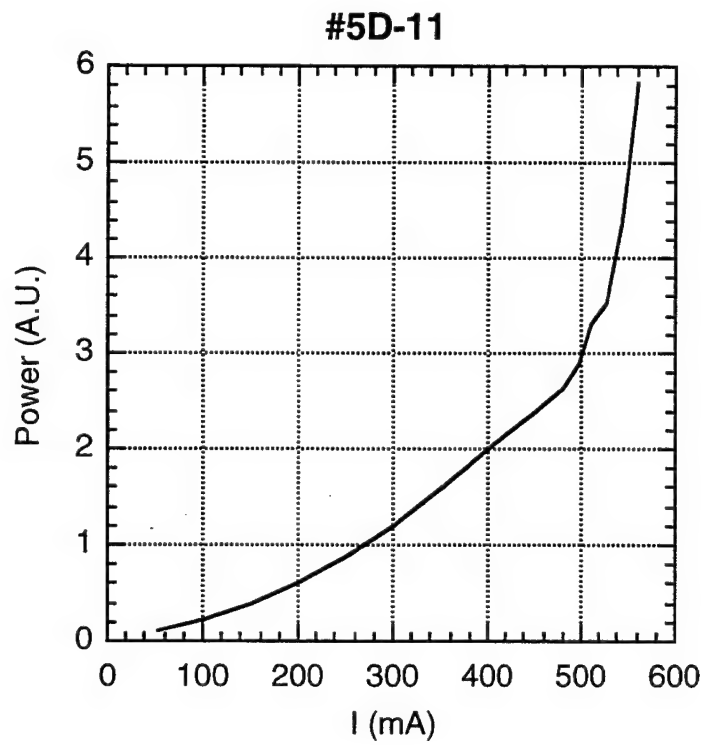


**Figure 9:** Laser power versus injection current after Zn implantation, annealing and 2 minutes Zn diffusion

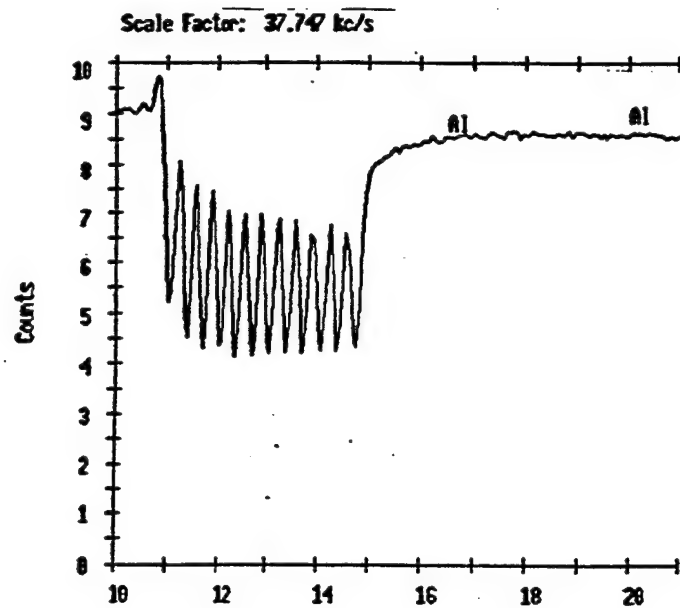


Figure 10: SIMS Al profile for as grown sample

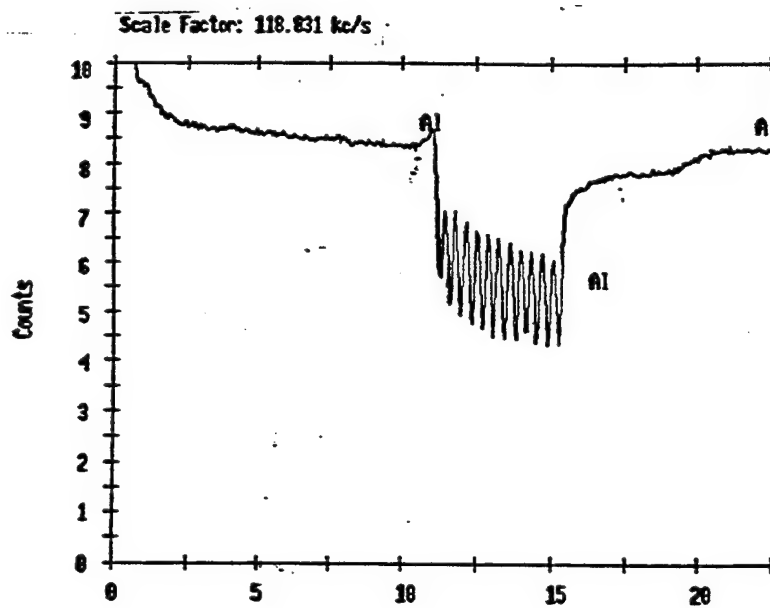


Figure 11: SIMS Al profile after implantation, annealing and diffusion  
Note scale factors



at 700 °C was necessary after implantation and annealing to form ohmic contacts and to give the correct p-type doping profile.

Figure 9 shows the P versus I curve for a laser structure of dimension 50x500 microns. The threshold current density is 2000 A/cm<sup>2</sup>. SIMS profiles of Zn and Al in these laser structures (Figure 10 and 11) show that the MQW is only partially intermixed and would account for the relatively high threshold current density of the laser section.

### **Tapered Waveguide Interconnect:**

#### **Impurity Induced Layer Disordering:**

Quantum well mixing, or impurity induced layer disordering ( IILD ) as it is also known, is potentially an important new technology for the fabrication of photonic and optoelectronic devices in quantum well structures. Since the shape of the quantum well determines the properties of the quantum well, this technology, which effectively allows the well profile of selected parts of the sample to be modified, could be utilized to fabricate novel optical devices. It has the advantages of a planer device technology and could be used for the fabrication of three dimensional devices, and hence greatly simplifying device processing. Although this process was first demonstrated in 1979, the mechanisms of the process are not well understood. Despite this lack of understanding, the process of IILD is already being used for the fabrication of some of the state of the art devices, such as quantum well lasers. Here we exploit the process of IILD to refractive index engineer a section of the MQW to fabricate a tapered modal interconnect.

Optical modal interconnects between devices on an OEIC chip require tailoring of band gap energies and therefore refractive indices of regions between the devices. This can be achieved by using IILD of the quantum wells [14]. IILD causes intermixing of Ga/Al, and has received considerable attention recently [15,16], as it also eliminates the need for regrowth in the fabrication sequence. We exploit a novel tapering technique, suitable for interconnecting a single quantum well (SQW) waveguide to a monolithic

# Before and after intermixing of layers

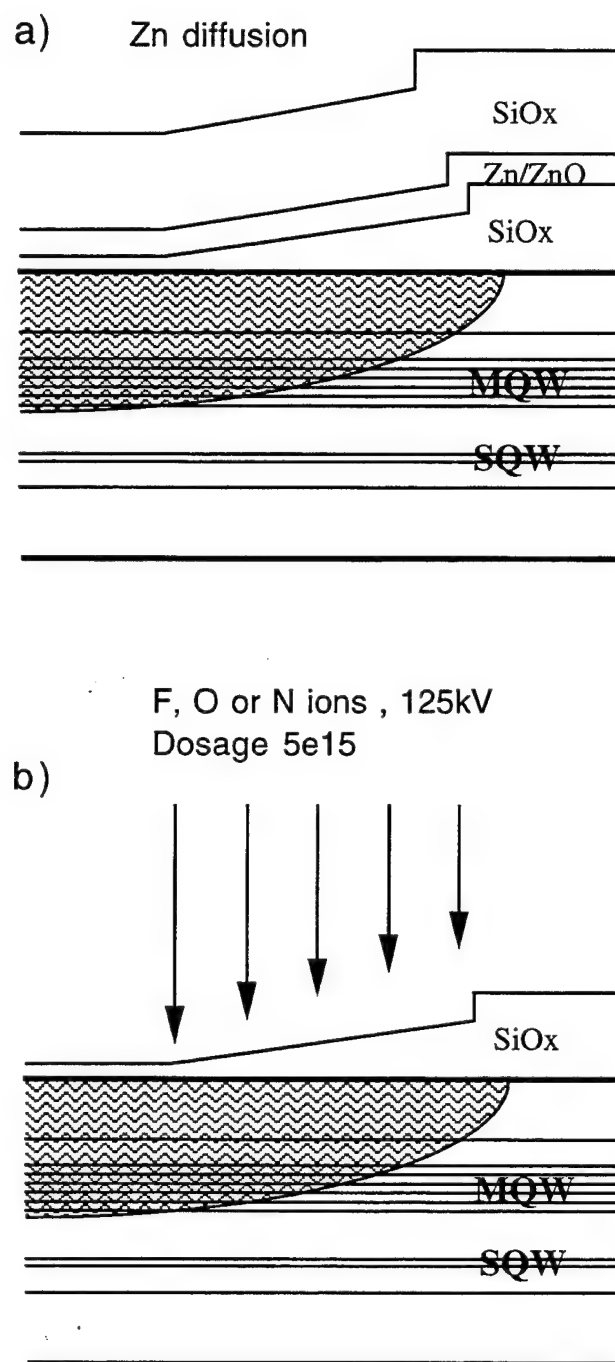
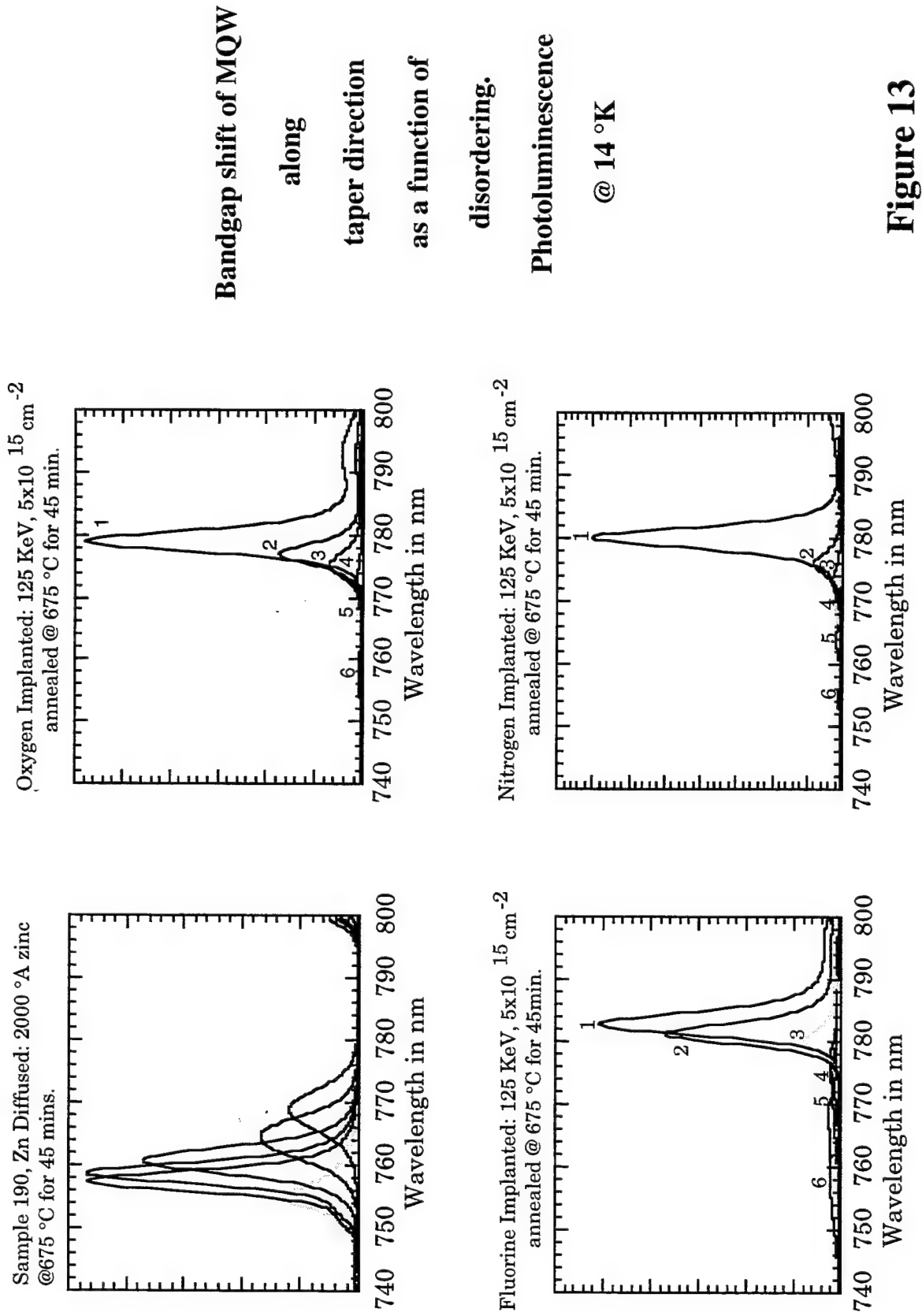


Figure 12 a,b: Schematic of process of IILD by Zn diffusion and F,O,N implantation and annealing

**Figure 13**

multi-quantum well (MQW) waveguide, using IILD of the MQW region via Zn diffusion or impurity implantation through a tapered  $\text{SiO}_x$  barrier layer on the MQW waveguide. In the case of Zn diffusion, the Zn concentration profile along the growth direction, in the MQW waveguide, is determined by the thickness of the  $\text{SiO}_x$  barrier layer. Since the thickness of  $\text{SiO}_x$  barrier varies slowly along the propagation direction, so does the diffused Zn profile. Zn diffusion into the MQW waveguide intermixes Ga and Al ions through group III vacancy generation via a 'kick out' mechanism so that the quantum wells are gradually destroyed. This results in blue shifting of the absorption edge, i.e. the band gap of the MQW increases, while simultaneously decreasing the refractive index of the MQW region, since the effective Al concentration in the wells increases. The extent of blue shifting the band gap and decreasing of the refractive index of the MQW can be controlled by varying the concentration of Zn diffusant through variation of thickness of the  $\text{SiO}_x$  barrier layer.

The process of impurity induced layer disordering of the MQW region of the monolithic structures is shown in figure 12 a,b. The process of taper fabrication consists of a) deposition of  $\text{SiO}_x$  layer with a thickness varying linearly from 0 to 300 nm along a 3-mm length, followed b) deposition of Zn, c) deposition of a capping  $\text{SiO}_x$  layer, and finally d) diffusion of Zn into the MQW section via annealing at 675 °C for 30 minutes or alternatively by Fluorine, Oxygen or Nitrogen implantation at an energy of 125 kV with a dosage of  $5 \times 10^{15}/\text{cm}^2$  and subsequent annealing at 675 °C for 30 minutes.

Figure 13 shows the Photoluminescence (PL) spectra, across the taper formed after Zn diffusion or F implantation and annealing in structure A, and the spectra in structure B after O, N implantation and subsequent annealing, measured at 14 °K. It shows that the extent of blue shift of the band gap of the MQW correlated well with thickness of the  $\text{SiO}_x$  barrier layer. From the temperature dependence of the MQW PL peak position of the as-grown sample, we estimated value of the bandgap of the MQW at room temperature to be 1.494 eV (0.83  $\mu\text{m}$ ).

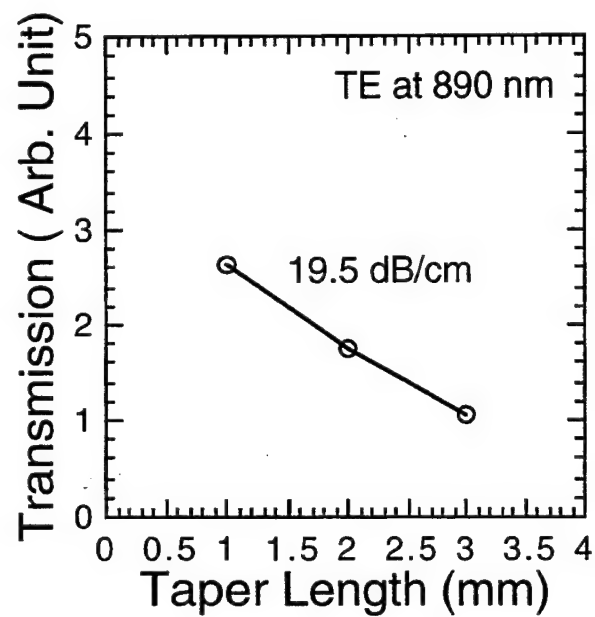


Figure14a: Propagation loss in taper formed by F implantation

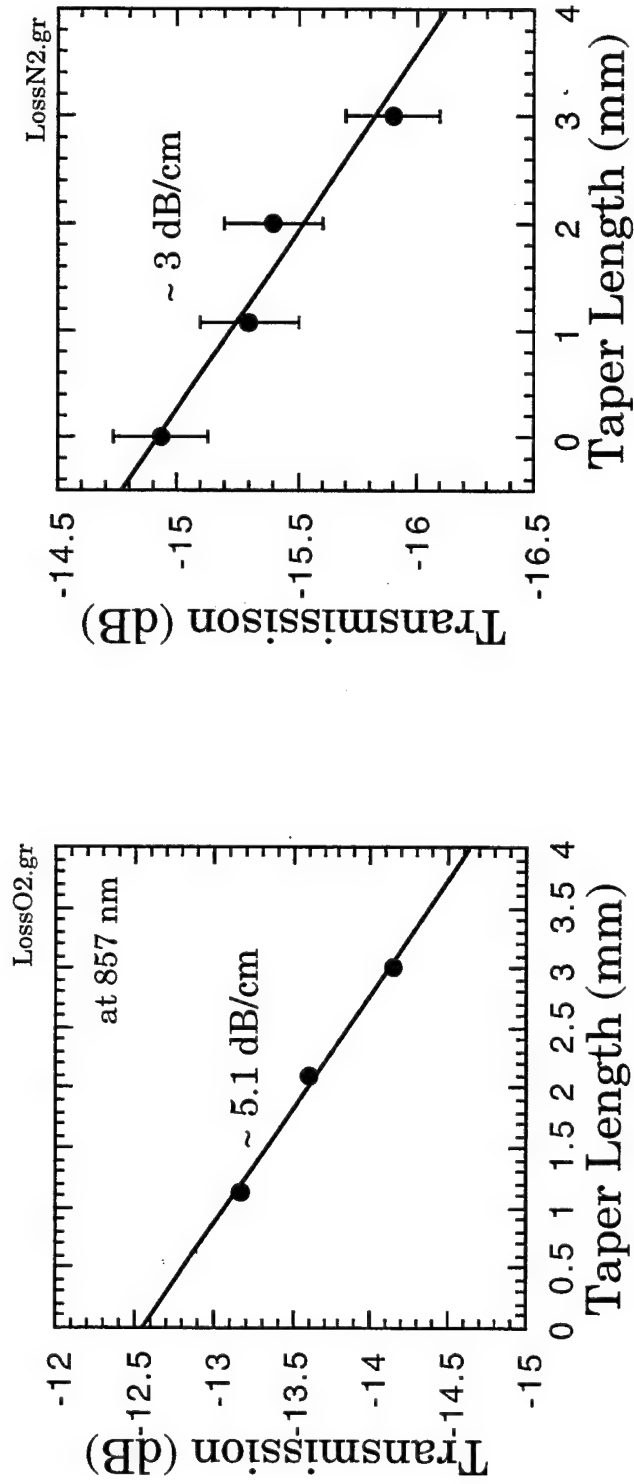


Figure 14b: Propagation loss in taper formed by O and N implantation

### **Propagation Loss Measurement:**

For measurements of waveguide propagation loss due to F, O or N implantation, ridge waveguides of 6 microns width and 0.8 microns height were fabricated in structure A for the case of F implantation and in structure B for the case of O and N implantation, after annealing the samples at 675 °C for 45 minutes. Since the propagation loss of the tapered waveguide structure varies along the beam propagation direction we used samples implanted without the tapered SiO<sub>x</sub> barrier, to avoid complicated calculations. The conventional cutback method was used to measure the waveguide propagation loss using TE polarized light 0.89 μm. Figures 14 a,b,c show the measured propagation losses for the case of F, O and N respectively. In the case of a tapered waveguide interconnect, the loss brought about by F implantation along the beam propagation direction varies from 0 to 18 dB/cm. By taking an average along the beam propagation direction, the average propagation loss of the device is around 9 dB/cm.

### **Refractive Index change due to Zn IILD:**

There is considerable interest in IILD of quantum well structures due to their potential application in device integration without having to utilize complex regrowth processing. IILD alters the compositional profile of the quantum wells from a rectangular well to a non rectangular shape. The alteration of the compositional profile of the well structure and the modification of its band structure causes a variation in the refractive index of the quantum wells. However, very little work has been done in the measurement of refractive index variation in quantum well structures, especially in MQW structures which are useful in device applications. Here we present measurements of the refractive index variation of a Zn diffused GaAs/AlGaAs MQW structure for TE polarized light.

An MQW structure consisting of 70 pairs of 19 nm thick Al<sub>40</sub>Ga<sub>60</sub>As barriers with 6.5 nm thick GaAs wells was grown on a semi insulating GaAs substrate. The absorption edge of this structure was measured to be at 0.83 microns at room temperature.

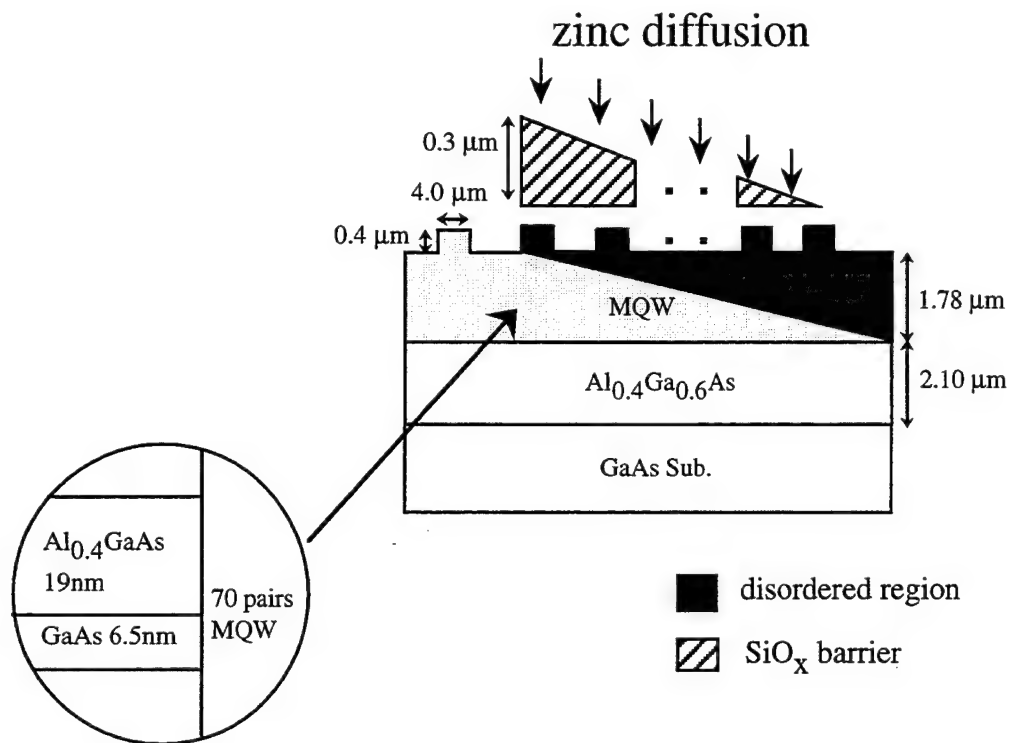


**Figure 15:** Cross section of MQW sample used in interference measurements



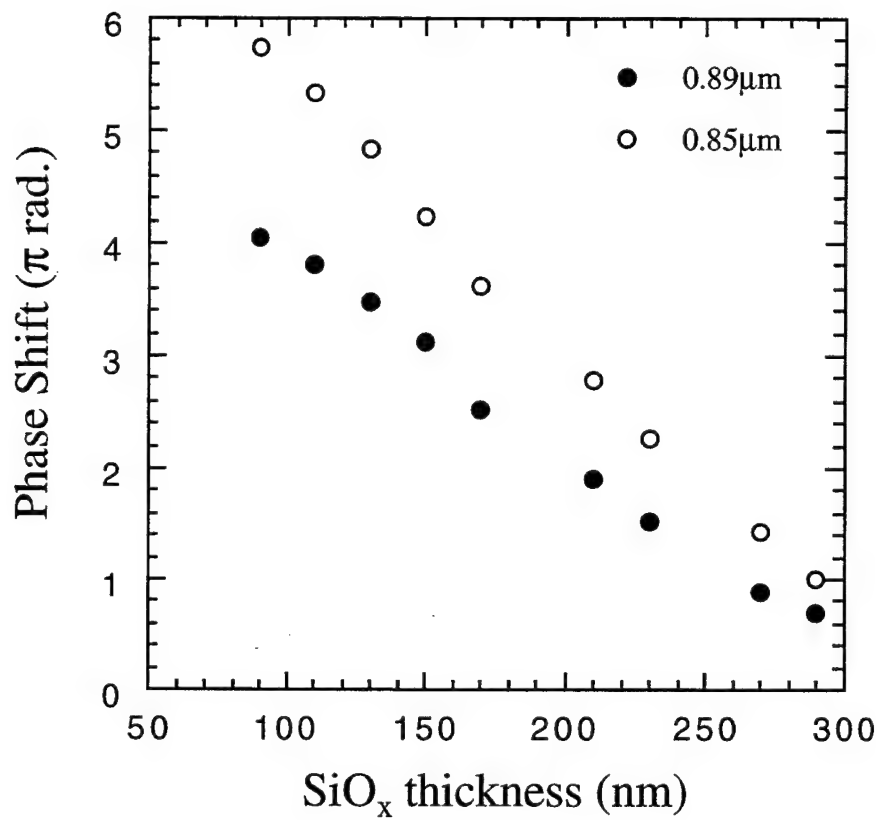


Figure 16: Measured phase shift versus SiO<sub>x</sub> thickness.

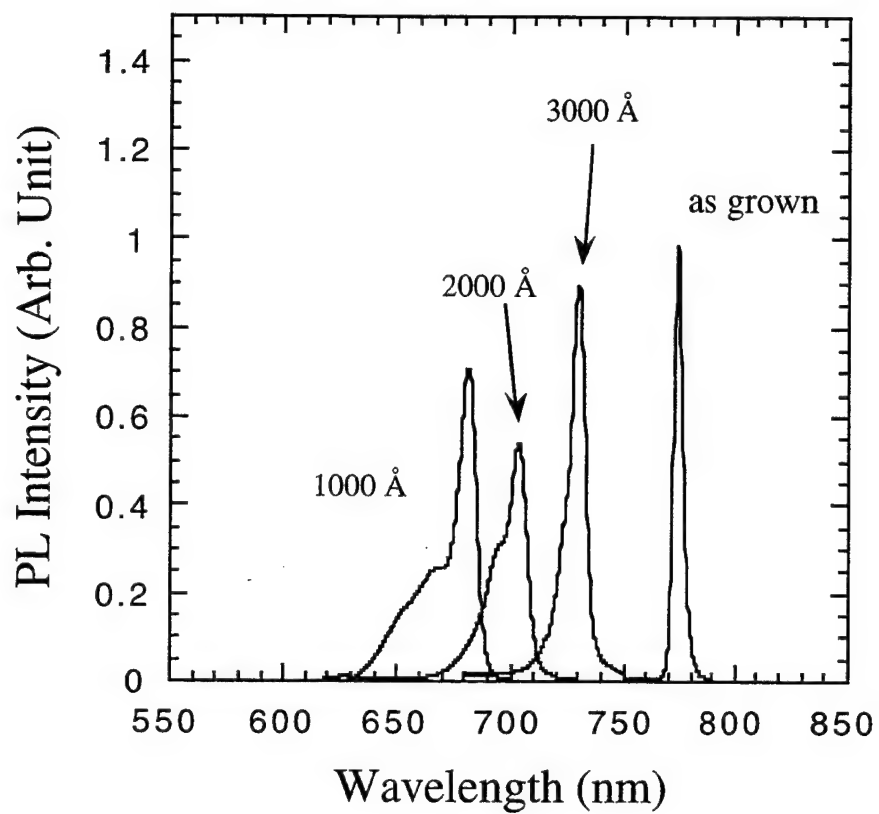


Figure 17: Zn IILD induces blue shift of MQW peak

An interference technique was used to measure the mode index difference between waveguides on the MQW structure having different degrees of disordering. Figure 15 shows the lateral cross section of the structure having several uncoupled, ridge waveguides used in the interference measurements. The MQW waveguides with different amounts of interdiffusion were fabricated by diffusing Zn through a tapered  $\text{SiO}_x$  barrier as mentioned before. As a relatively large index change was expected, on the order of  $1e-3$  between adjacent waveguides, only a small section of the waveguides along the longitudinal direction was disordered to resolve the mode index variation within one fringe shift.

After the sample was cleaved to a length of 3 mm, Mach-Zehnder interference measurements were done using TE polarized light at 0.85 and 0.89 microns using a tunable Ti:Sapphire laser. The system is aligned such that the desired guided mode of a single ridge waveguide is excited and a vertical fringe pattern appears on the video camera. This requires interference of the defocused near field image of the waveguide with the reference beam on the video camera until the two wavefronts have the same curvature. One of the horizontal lines of the video signal is then scanned and saved in a storage oscilloscope. Similar measurements were done on the complete set of ridge waveguides sequentially.

The phase difference between two consecutive waveguides is given by

$$\Delta\Phi = 2\pi (N_i - N_{i-1})L / \lambda$$

where  $N_i$  represents the mode index of the  $i$ th waveguide and  $\lambda$  is the source wavelength.  $L$  is the length of the Zn diffused region. The total phase change of each individual waveguide was obtained by adding consecutive phase differences starting from the undisordered waveguide. Figure 16 shows the measured phase shifts as a function of  $\text{SiO}_x$  thickness at two different wavelengths.

We used PL spectroscopy to measure variations in the energy levels of the MQW with varying degrees of disordering. Figure 17 shows the PL spectra from disordered

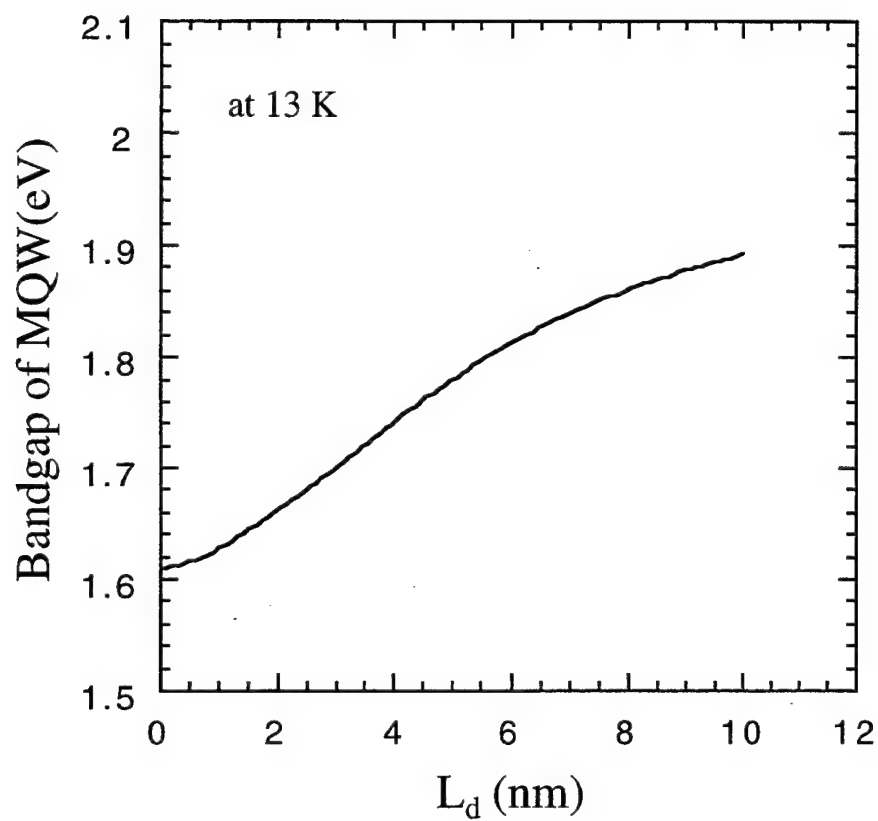


Figure 18: Calculated band gap variation of MQW versus  $L$

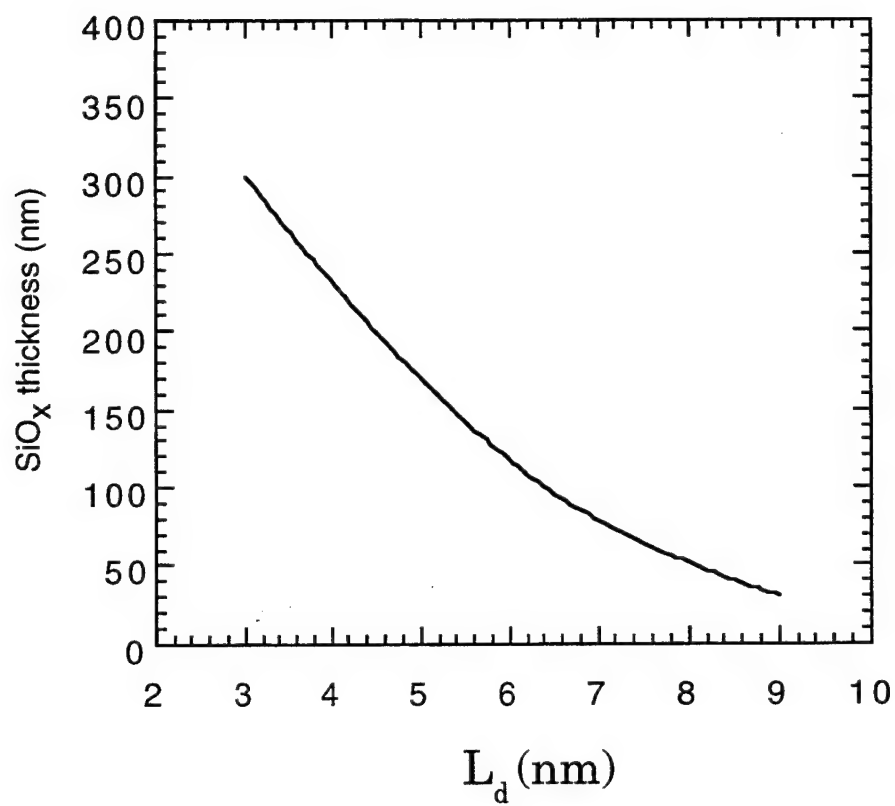


Figure 19: The relationship between the  $\text{SiO}_x$  barrier thickness and  $L_d$

regions with different  $\text{SiO}_x$  barrier thickness. A correspondance between the blue shift of the PL peak position with decreasing thickness of the  $\text{SiO}_x$  barrier layer is evident. The relation between the interdiffusion length of Ga/Al and the  $\text{SiO}_x$  barrier thickness were obtained by comparing the theoretically calculated energy level shifts, which utilized a variational method, due to the interdiffusion of Ga/Al to that obtained from PL measurements. The calculated band gap variation of the quantum well as a function of  $L_d$  is plotted in figure 18. Therefore, the relation between the  $\text{SiO}_x$  barrier thickness and  $L_d$  can be determined by comparing the measured PL peak positions at different  $\text{SiO}_x$  thickness to the calculated band gap variation as a function of  $L_d$ . The obtained correspondance between the  $\text{SiO}_x$  barrier thickness and  $L_d$  is represented in figure 19.

In order to obtain the variation of refractive index of the MQW due to Zn diffusion, we assume that the refractive index of the interdiffused MQW waveguides are represented by an equivalent step index rather than the graded index profile. Since the PL peaks under different barrier thicknesses shifted significantly but with a relatively small broadening, we believe that the variation in the degree of disordering from the top to the bottom of the MQW is relatively small in our diffusion process and therefore, our assumption is reasonable. Moreover, the ridge width (4 microns) of the waveguide is quite small compared to the taper length of 3000 microns. Thus, the step index assumption of the disordered region in the ridge waveguide is quite justified. Since the energy states in quantum wells change as a result of the disordering, this results in a blue shifting of the absorption edge and a variation in the absorption spectrum near the band edge. The refractive index of the MQW near the band edge decreases with increasing disorder. The mode index change between adjacent waveguides can be obtained from the measured phase difference and is given by

$$\Delta N = (\lambda / 2 \pi L) \Delta \Phi$$

where  $\Delta N$  is the mode index change,  $\lambda$  is the wavelength,  $\Delta \Phi$  is the phase difference, and  $L$  is the length of the Zn diffused region. Therefore, a phase difference  $\pi$  between

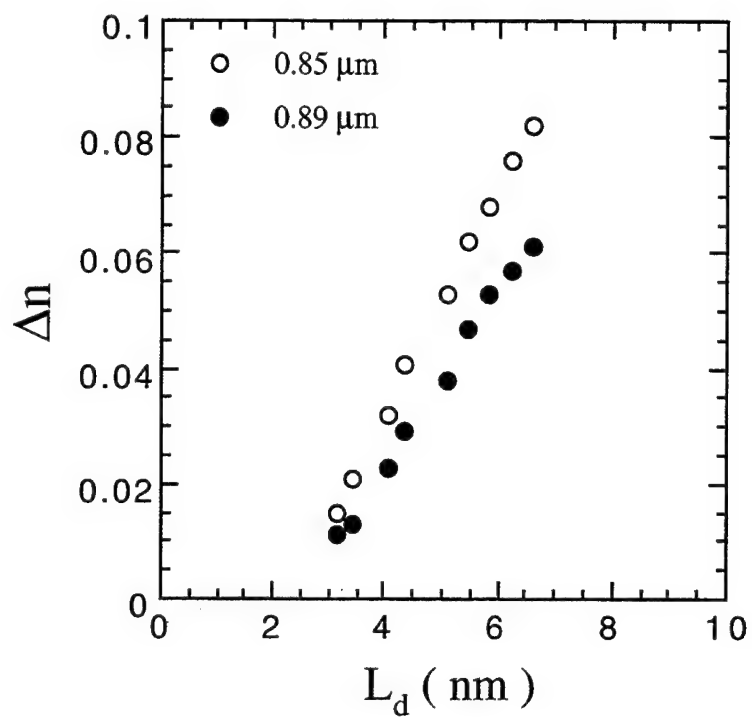


**Figure 20:** Calculated  $\Delta n$  versus  $L_d$

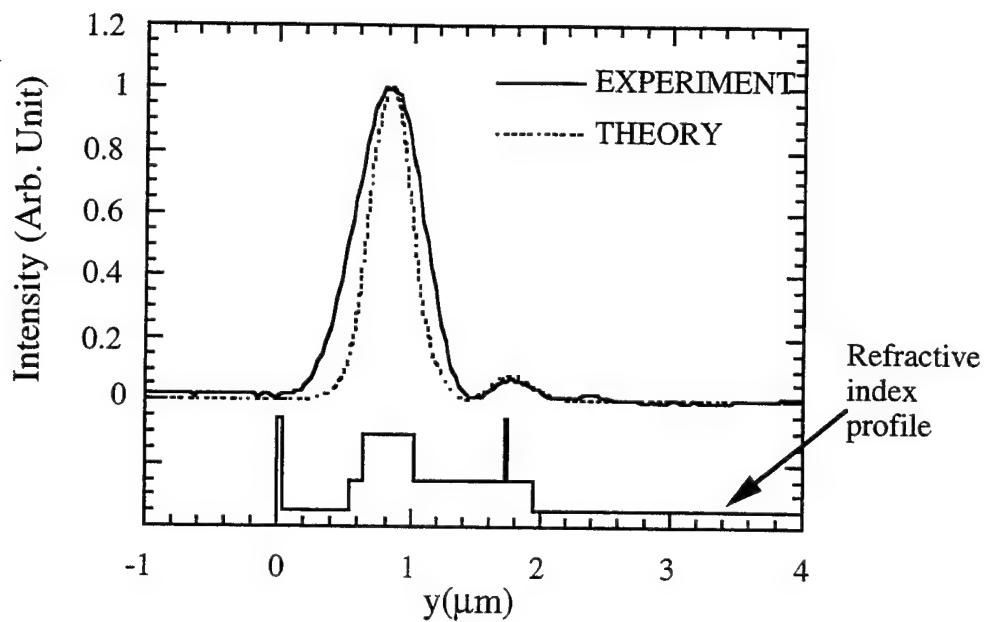
waveguides for  $L=30$  microns corresponds to a  $\Delta N = 0.0148$  and  $0.0142$  at  $\lambda = 0.89$  and  $0.85$  microns, respectively. In order to deduce the refractive index variation ( $\Delta n = n_{\text{undisordered}} - n_{\text{disordered}}$ ) from the measured  $\Delta N$ , an effective index analysis of a step index three- layer ridge waveguide (AlGaAs/MQW/Air) was used. The refractive index of the undisordered MQW is assumed to be equivalent to that of an AlGaAs alloy which has the same bandgap energy as the MQW. The refractive index of the AlGaAs alloy was calculated using the equations from Afromowitz [17]. For the undisordered MQW ridge waveguide structure, we calculate the mode index  $N_{\text{undisordered}}$  for the fundamental mode. The mode index of the ridges which have disordered wells is equal to  $N_{\text{undisordered}} - \Delta N$ , where  $\Delta N$  is the measured change in the mode index.  $\Delta n$  is then determined by using an iterative process, from the new mode index  $N_{\text{undisordered}} - \Delta N$ . The calculated  $\Delta n$  of the MQW, from the measured  $\Delta N$  is plotted in figure 20 as a function of disordering due to interdiffusion. We use  $L_d$  to represent the extent of disordering.

#### **Origin of $\Delta N$ in disordered MQW of monolithic structure:**

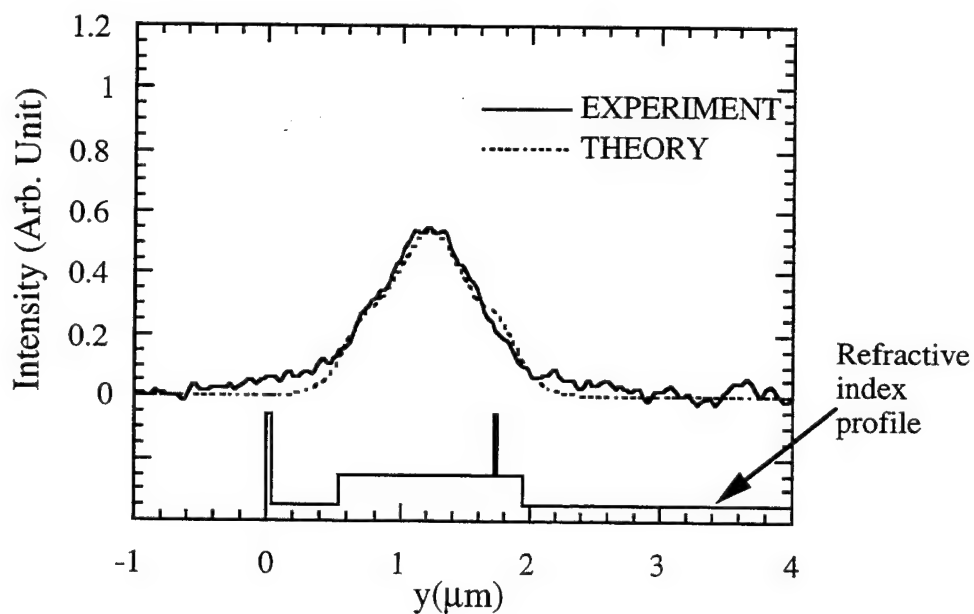
In order to separate the contribution of the free carrier induced change and the IILD induced change to the refractive index of the MQW, two measurements were performed. Mode index measurements [18] at  $1.3 \mu\text{m}$  were used to determine the free carrier induced index change. For these measurements ridge waveguides were photolithographically defined and etched perpendicular to the tapered, Zn disordered direction of an MQW sample. The mode index change at  $1.3 \mu\text{m}$  ( $\Delta N$ ) was evaluated to be  $0.0014$ . This small value of  $\Delta N$  implied that the free carrier contribution to the refractive index change is rather small and hence can be neglected.

Near field intensity measured at  $0.895 \mu\text{m}$  was used to determine the IILD induced index change. A tunable Ti:Sapphire laser ( $0.895 \mu\text{m}$ ) was used to excite the guided modes of the composite structure for both the as-grown and Zn diffused sample. The solid curve in Fig.21(a) shows the measured output intensity profile along the growth





(a)



(b)

Intensity profiles from both ends of the taper. a). Near field profile of as grown sample. b). Near field profile of the disordered section. Solid curves represent measured profiles, dotted curves numerically calculated profiles, and solid lines under the profiles the index profile along the depth direction.

**Figure 21**

direction of the as-grown sample. Almost 95% of the power is concentrated in the MQW region with a small lobe around the SQW region. The solid curve in Fig.21(b) shows an output intensity profile measured at the disordered end of the Zn diffused side with light launched into the undisordered end, propagating along the 3mm-long tapered section. It shows a broader profile than that in Fig.21(a) and is a direct consequence of the refractive index decrease in the disordered MQW due to the IILD process.

### **Modeling and Analysis of Tapered Waveguide Interconnect:**

We will demonstrate an adiabatically tapered MQW by z-variant impurity induced layer disordering caused by Zn diffusion through an  $\text{SiO}_x$  barrier layer whose thickness varies linearly along a longitudinal direction. This analysis utilizes the step transition model and multilayer stack theory to establish the adiabatic nature of the tapered structure [19]. In this analysis, the refractive index of the MQW waveguide was determined by evaluating an equivalent  $\text{Al}_x\text{Ga}_{1-x}\text{As}$  alloy, corresponding to the MQW bandgap energy along different segments of the taper. Based upon our theoretical and experimental results, we propose a modified epilayer structure to reduce coupling loss between laser and taper sections and to achieve higher modulation efficiency. This modification employs the concept of tapered, both in index and in dimension, velocity couplers and is used in the integration of the SQW laser to the MQW intensity modulator.

The first bound state energy levels of the electron and heavy hole were calculated using a 0.6:0.4 conduction band ( $\Delta E_C$ ) to valence band ( $\Delta E_V$ ) offset ratio. This gives an  $E_g(\text{MQW})$  of 1.494 eV, which is essentially the value obtained from the PL measurements. The refractive index of the  $\text{Al}_x\text{Ga}_{1-x}\text{As}$  alloy for all relevant values of  $x$ , at  $0.895 \mu\text{m}$  was analytically calculated using the following equations [17],

$$n^2 - 1 = \frac{E_d}{E_o} \left( 1 + \left( \frac{E}{E_o} \right)^2 + \frac{E^4}{2E_o^2(E_o^2 - E_g^2)} \ln \left( \frac{2E_o^2 - E_g^2 - E^2}{E_g^2 - E^2} \right) \right) \quad (1)$$

where

$$E_0 = 3.65 + 0.871x + 0.179x^2 \quad (2)$$

$$E_d = 36.1 - 2.45x \quad (3)$$

$$E_g = 1.424 + 1.266x + 0.26x^2 \quad \text{for } (0 \leq x < 0.4) \quad (4)$$

$$E = hc/\lambda \quad (\lambda: \text{wavelength}) \quad (5)$$

Substituting the value of  $E_g(\text{MQW})$  into Eq. 4 gives the Al mole fraction ( $x$ ) of the  $\text{Al}_x\text{Ga}_{1-x}\text{As}$  alloy equivalent to the undisordered MQW and is  $x=0.05$ , which is then used in Eqs. 2 and 3. Finally, the refractive index of the MQW as calculated from Eq. 1 is 3.553. The solid line under the intensity profile in Fig.21(a) shows the refractive index profile across the sample of structure A and includes the equivalent refractive index for the MQW waveguide. The refractive index for the most disordered section of the MQW was calculated similarly except that the Al mole fraction of an equivalent  $\text{Al}_x\text{Ga}_{1-x}\text{As}$  alloy is calculated from Eq. 6.4 using measured bandgap values obtained from the PL spectrum. A totally disordered MQW would have an equivalent Al mole fraction of  $x=0.298$ ; but the PL spectrum indicates that the peak of the most disordered MQW remains at a higher wavelength region than that of the cladding  $\text{Al}_{0.25}\text{Ga}_{0.75}\text{As}$  layer. Hence the actual refractive index of the most disordered MQW is slightly higher than that of the cladding. The solid line in Fig.21(b) under the intensity profile shows the refractive index profile of the most disordered MQW.

For a given step index profile, multilayer stack theory gives the mode index as well as its field profile [19]. We find that three normal modes can be guided in the as-grown structure A; we can fit the measured output intensity profile with a combination of the calculated guided modes. The best fitted intensity profile is shown in Fig.21(a) as the dotted curve, which is obtained from  $(\epsilon_0(y))^2 + (0.45\epsilon_2(y))^2$  where  $\epsilon_i(y)$  represents the field profile of the  $i$ -th mode. The first order mode does not contribute to the intensity profile due to the input excitation condition. We believe that the difference in modal depth between the measured and calculated profile is partially due to a minor variation in the Al mole fraction and thickness of the layers as well as due to value of the refractive

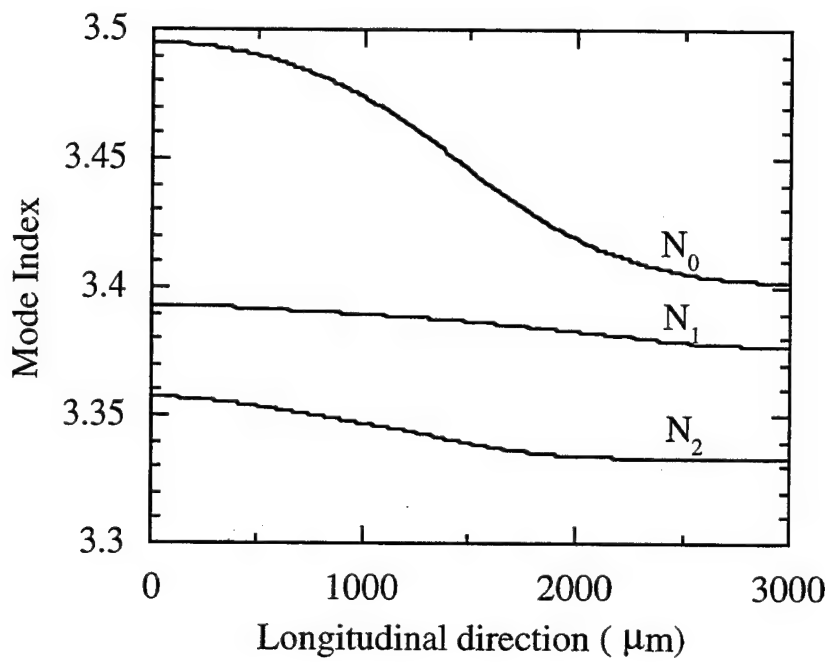
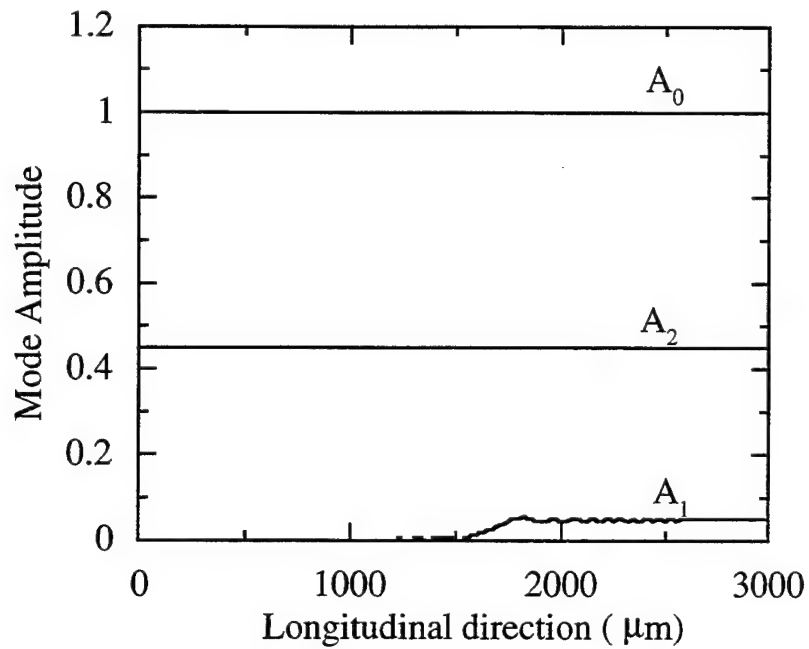


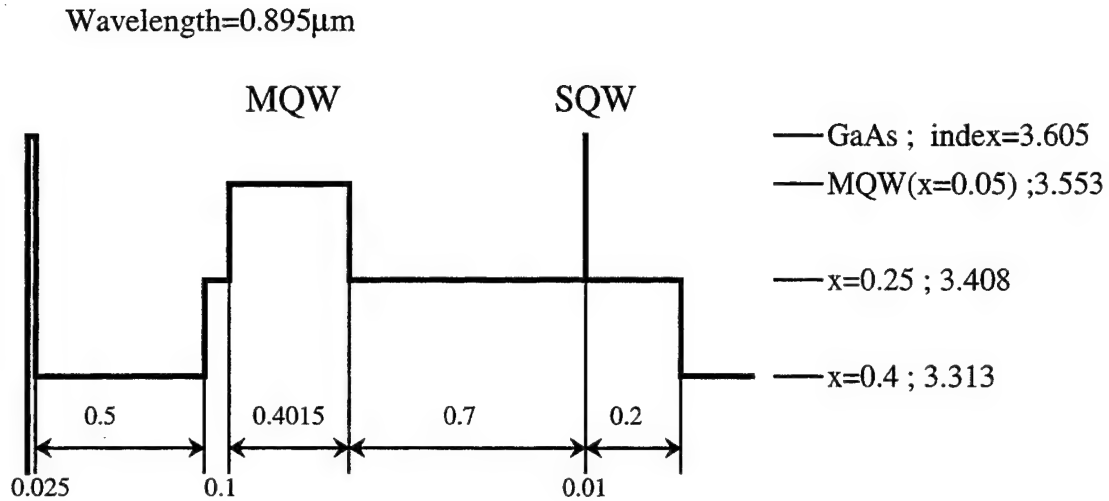
Figure 22: Mode indices along the taper.



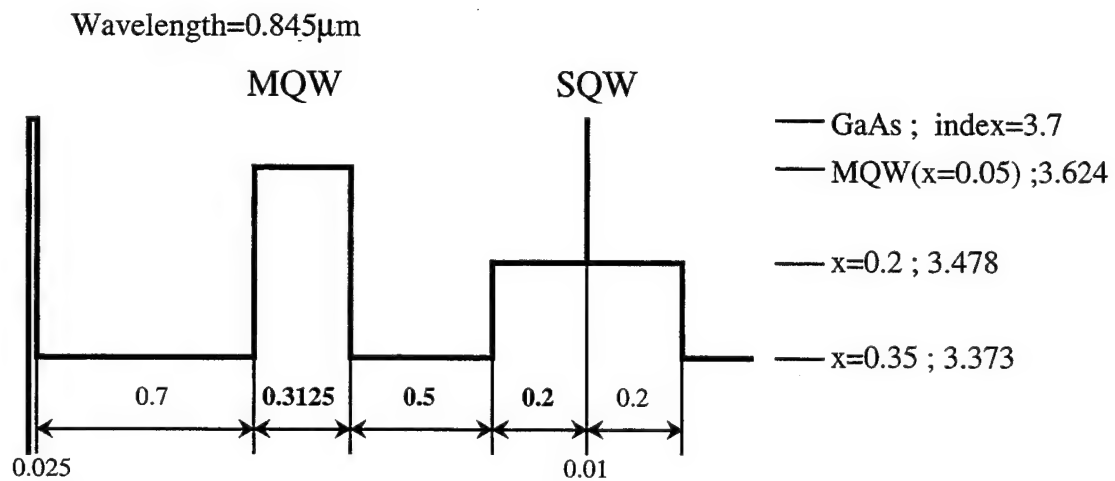
Mode amplitudes along the tapered structure, calculated from the step transition model with input amplitudes of the fundamental and second order mode as  $A_0 = 1$  and  $A_1 = 0.45$ .

Figure 23

index for the MQW which is not corrected to incorporate the effect of the excitonic peak in the absorption spectra. For the most disordered MQW case, there should be no excitonic peak present in its absorption spectra, and hence a better fit is obtained (Fig.21(b)). To analyze the tapered section, we utilize the step transition model [20,21,22] combined with the multilayer stack theory. In the tapered section, the slowly varying Zn and hence the refractive index profile can be approximated by a piecewise linear profile. The abrupt step separates two adjacent segments of different refractive indices. Within each segment, we assume a constant index value. The refractive index decrease due to Zn in the disordered MQW is assumed to be proportional to the concentration of Zn. The Zn concentration profile along the growth direction in the MQW region is assumed to be linear. The minimum value of the refractive index of the disordered MQW region is set to be slightly larger than that of the cladding, and is illustrated by the solid line in Fig.21(b). At each segment, the mode indices are calculated and are shown in Fig.22. In addition, the field profiles of the guided modes needed for the calculation of the overlap integral between the modes, across the step, and between the segments are also evaluated. The normal mode amplitudes along the entire device length are then calculated, following the procedure of the step transition model [19] using local normal modes. The loss is primarily due to free carrier generation by IILD (12dB), and the taper loss is estimated to be negligible. As is shown in Fig.23,  $A_0$  and  $A_2$  ( $A_i$ :i-th mode amplitude) at the input were set to be 1.0 and 0.45, respectively. The values were obtained from the best fit presented in Fig.21(a). As the combined modes travel along the tapered transition, almost no mode conversion occurs thus establishing the adiabatic operation of the taper transition. Note that while the power is associated with the term  $\sum(A_i)^2$ , the intensity profile is represented by  $\sum(A_i \epsilon_i(y))^2$ . The dotted curve in Fig.21 (b) was plotted using  $\sum(A_i \epsilon_i(y))^2$  with the  $A_i$ 's calculated at the output; it shows excellent agreement with the experimental results.



(a)



(b)

Refractive index profile of the as grown sample for:

a) the old structure

b) the modified structure for optimum operation of taper

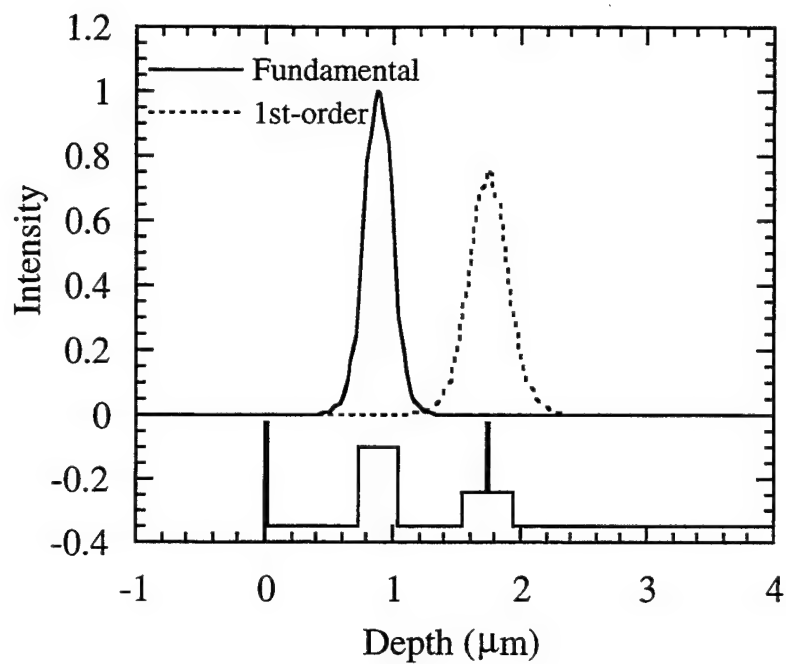
Figure 24

### **Optimization of the Taper Modal Evolution:**

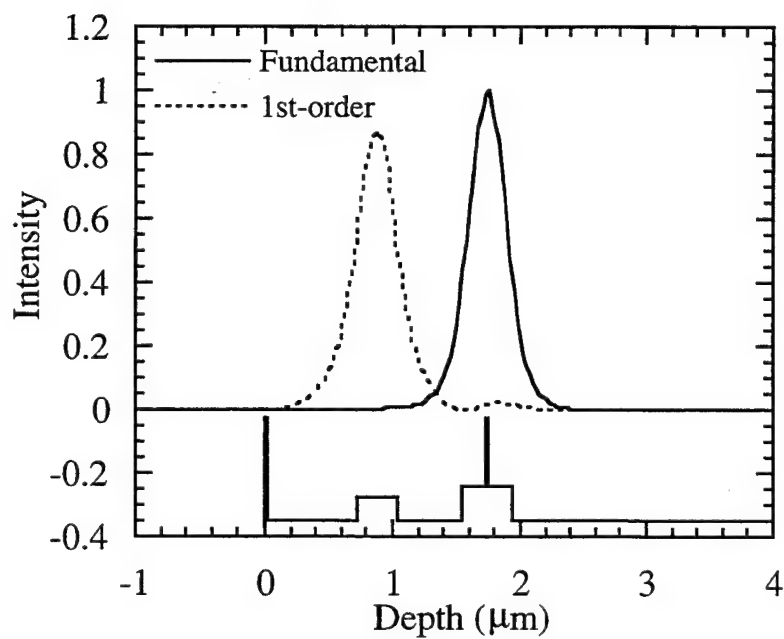
The main objective of our tapered interconnect is to completely transfer power from the SQW laser section to the MQW modulator. In that sense, the structure shown in Fig.2(a) was designed to achieve better mode sorting at both the ends of the taper. A schematic index profile of the previous epilayer structure is illustrated in Fig.24(a) at a wavelength of  $0.895\text{ }\mu\text{m}$ . Though there is no mode conversion used for the interconnect (Fig. 23), the input beam from the SQW laser could not be coupled into the fundamental mode of the disordered section. This is primarily because the mode from the SQW laser has a narrow peak centered at the SQW while the fundamental mode of the disordered section has a broad peak at about the center region of a big pedestal waveguide which consists of the disordered MQW, the SQW, gap between them,  $\text{Al}_{0.25}\text{Ga}_{0.75}\text{As}$  layers below the SQW and above the MQW region. Accordingly, power at the output (as-grown) section is not concentrated in the MQW region.

An optimized epilayer structure is presented in Fig.24(b) with its schematic depth refractive index profile. The operating wavelength was chosen to be  $0.845\text{ }\mu\text{m}$  at which wavelength the MQW absorption modulator shows the best extinction ratio [23]. The thickness of the SQW will be determined later because fine tuning of a lasing wavelength will invariably involve an experimental trial-and-error procedure. Besides, the thickness of the SQW does not have much effect on the performance of the taper and the modulator sections. The refractive indices of all epilayers were calculated again for the new operating wavelength using Eqs. 1- 5. The pedestal waveguide was removed to suppress the third-order normal mode.  $\text{Al}_{0.2}\text{Ga}_{0.8}\text{As}$  layers of  $0.2\text{ }\mu\text{m}$  thickness are placed below and above the SQW for a better mode confinement in laser section. The number of quantum wells in the MQW is reduced to accommodate only one individual mode in the MQW region. The previous structure which has two individual modes had 15 GaAs quantum wells and 16  $\text{Al}_{0.4}\text{Ga}_{0.6}\text{As}$  barriers while the new structure has 13 barriers and 12 wells with same well and barrier thicknesses as well as the same Al mole fraction for





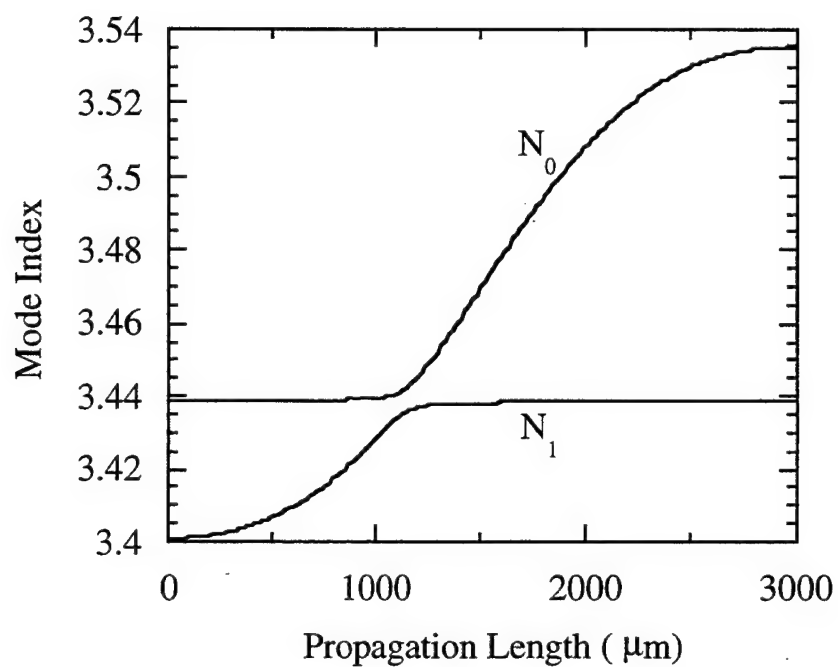
(a)



(b)

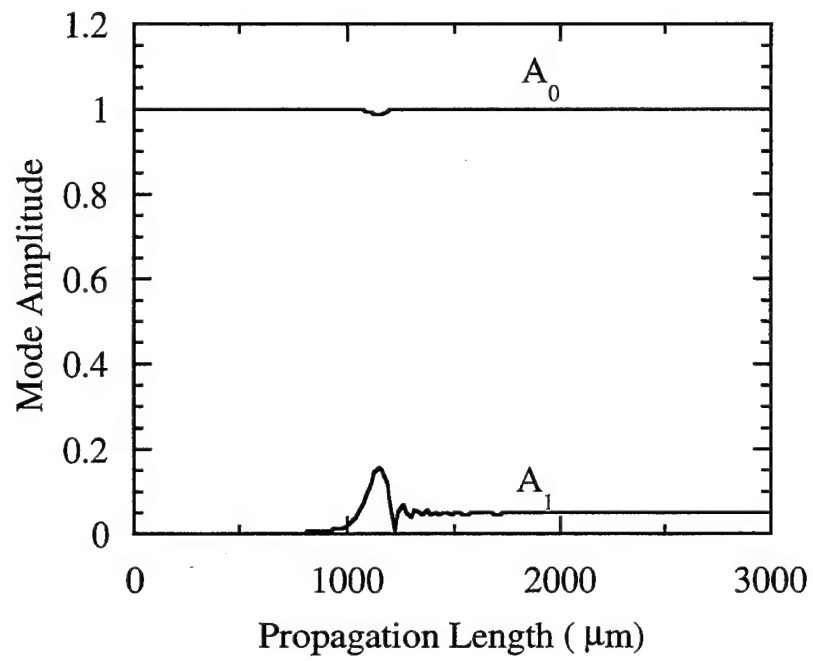
Intensity profiles of the first two normal modes of:  
a) undisordered region of the modified structure  
b) disordered region of the modified structure

Figure 25



Mode indices along the taper in the modified structure

Figure 26

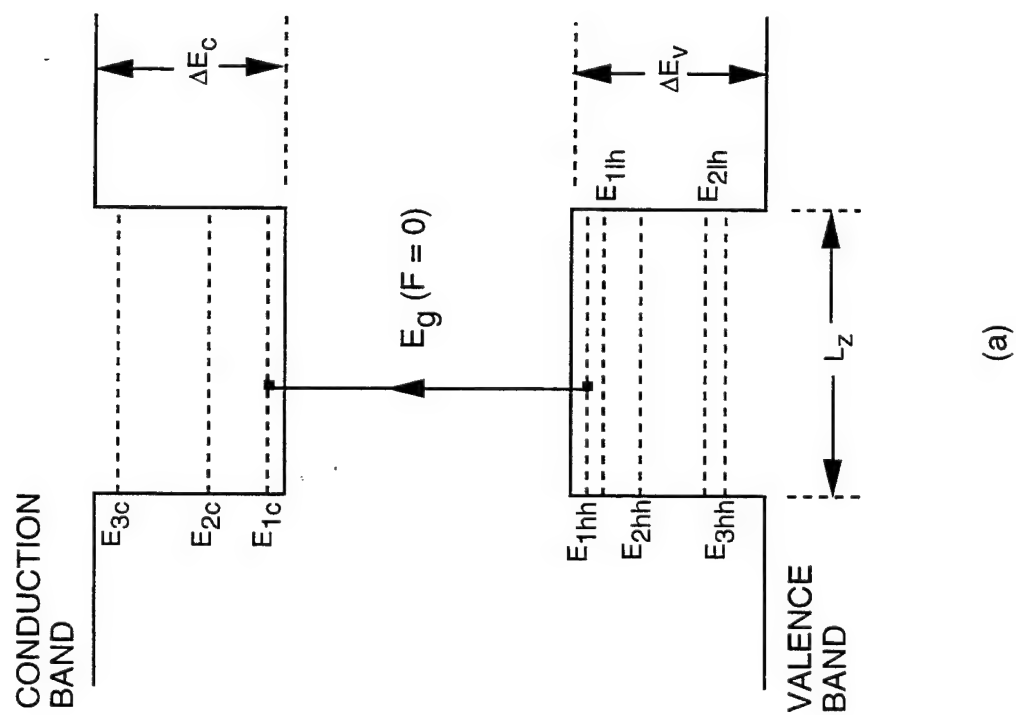


Mode amplitudes along the taper in the modified structure

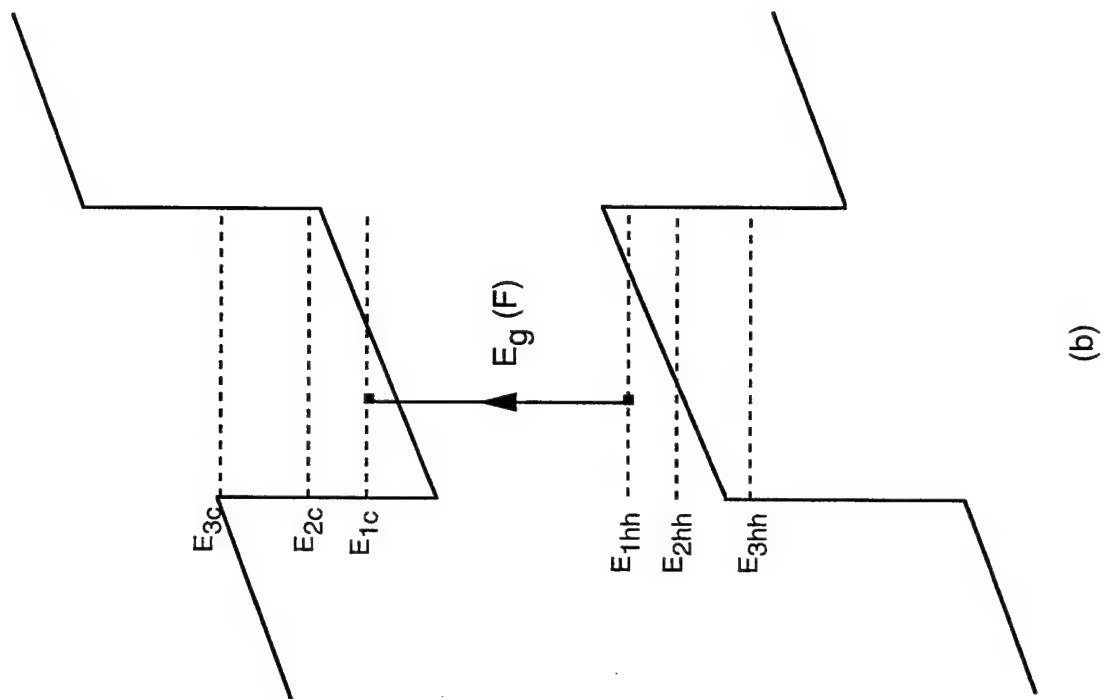
Figure 27

the barriers as the previous structure. Therefore, the bandgap for the MQW should remain unchanged. The position of the last well of the MQW region from the surface is not changed with expecting same extent of IILD effect, i. e., same amount of blue shift. Refractive indices for the gap between MQW and SQW guiding layers, and the thickness and refractive index of the guiding layers of the SQW are carefully chosen to facilitate mode sorting at the both ends of the taper without any mode conversion while propagating along a reasonable length (3mm) of the taper. The modified tapered interconnect, therefore, turns out to be a tapered, both in index and in dimension, velocity coupler which utilizes vertical coupling between the SQW guiding layers and z-variant MQW layers. Intensity profile of the first two normal modes for the as-grown and the disordered section of the new structure is shown in Figs.25(a) and (b), respectively. Solid lines in Figs.25(a) and (b) represent the index profiles for both the cases. The mode index change along the taper is shown in Fig.26. As can be seen from the figure, there is no third-order mode in this structure and almost perfect mode sorting is easily obtained. With input condition of  $A_0 = 1$  and  $A_1 = 0$ , mode amplitudes along the taper in the modified structure are calculated using the step transition model in conjunction with local normal modes and presented in Fig.27. The fundamental mode of the Fig. 25 (b) should be launched by SQW laser, then propagate with very little mode conversion (25dB), and finally end up with its complete energy content in the MQW region at modulator section, i. e., at the as-grown section, resulting in maximum modulator efficiency.

We have demonstrated an adiabatic, tapered transition in a monolithic integrated MQW and SQW coupled structure using Zn diffused IILD of the multi-quantum wells and have modeled the same. Numerical analysis shows excellent agreement with the experimental results. The taper length was 3 mm and at the two ends of the taper, namely, in the most disordered region and the undisordered region of the MQW, the Al mole fraction in the equivalent  $\text{Al}_x\text{Ga}_{1-x}\text{As}$  layer was  $x=0.298$  and  $x=0.05$ , respectively. This corresponds to an index variation of 0.14 across the taper. Modification of the



(a)



(b)

Figure 28: Band diagram of quantum well a) without, b) with an applied electric field perpendicular to the quantum well layers

tapered interconnect has been carried out by using the concept of a tapered, both in index and in dimension, velocity coupler which utilizes the vertical coupling between the SQW guiding layers and MQW layers. Numerical, normal mode analysis of the proposed, modified coupler predicts a better mode sorting behavior and hence complete power transfer from the MQW region into the SQW region.

### **MQW Modulator:**

Contemporary electroabsorption type optoelectronic modulators usually employ p-i-n epitaxial structures in which the optically active section consists of an intrinsic ( i ) region, composed of, alternating layers of very thin (  $\sim 10$  nm ) nominally undoped GaAs well layers and  $\text{Al}_x\text{Ga}_{(1-x)}\text{As}$  barrier layers. As the bandgap of  $\text{Al}_x\text{Ga}_{(1-x)}\text{As}$  is larger than that of the well, a modulation of the energy bands ensues in the direction of layer growth. This difference in energy gap between well and barriers confines the motion of electrons in the conduction band and holes in the valence band to the plane of the layers, giving rise to interesting quantum effects. This layered structure is referred to as a multiple quantum well ( MQW ) structure. When the barriers are of sufficient width (  $>> 10$  nm ) the wells can be treated as individual entities.

Figure 28a shows a schematic band diagram of such a quantum well ( QW ). The confinement of the carriers in the well results in discrete energy levels. In the valence band one actually obtains two sets of levels due to the different effective masses of heavy and light holes. The fundamental optical transition occurs between the highest heavy hole and the lowest electronic state.

If an electric field is applied perpendicularly to the layers, the bands tilt due to the potential of the external field, as shown in figure 28b, resulting in the shifting of the energy levels. This results in a smaller absorption energy and the absorption edge shifts to longer wavelengths, similar to the Franz-Keldysh effect known from bulk materials. Contrary to the Franz-Keldysh effect, however, the absorption edge retains its steep rise and excitonic character. This phenomenon in QWs is referred to as the quantum confined

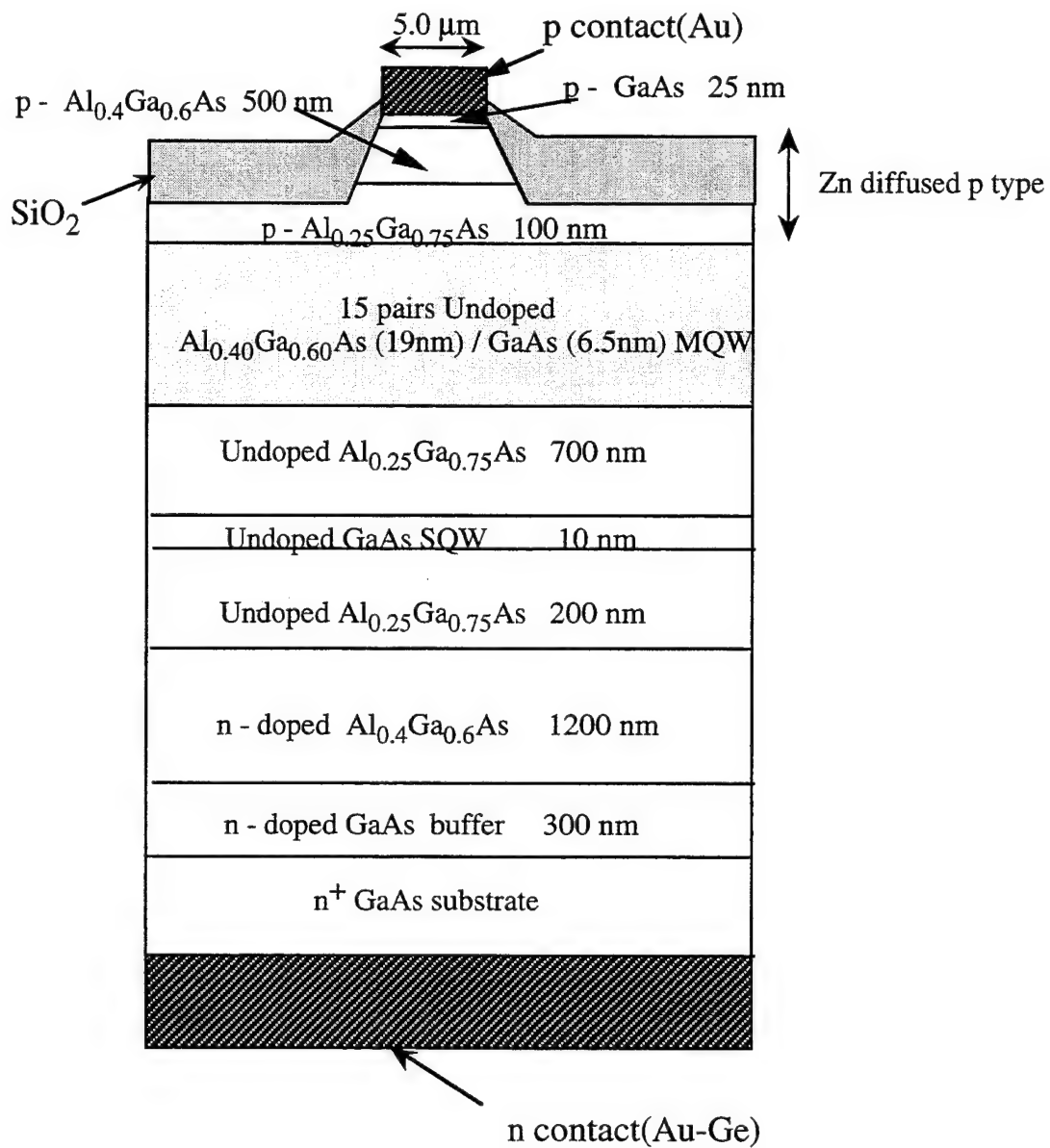


Figure 29: Cross section of structure A type MQW modulator

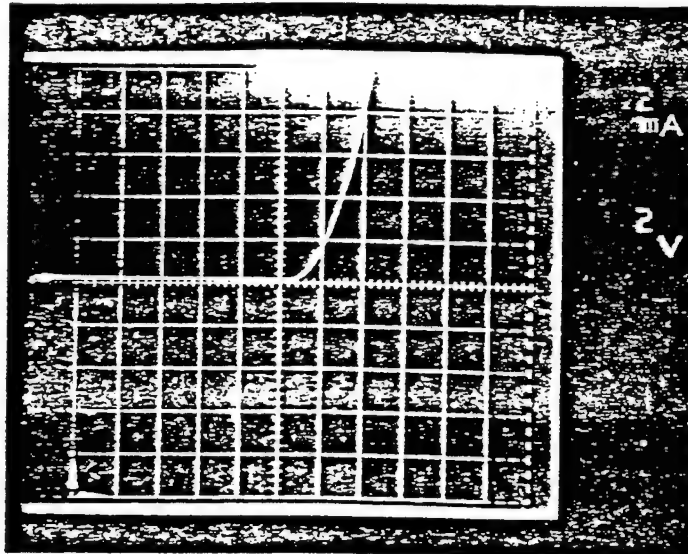


Figure 30: Current - Voltage characteristics of Modulator



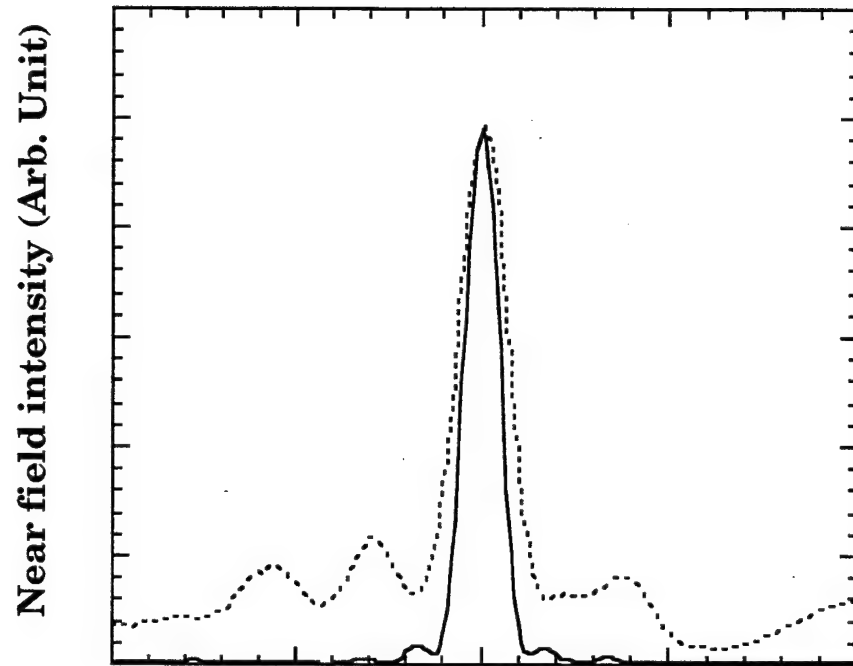


Figure 31: Horizontal and vertical near field intensity profiles of MQW modulator

Stark effect. It is this steep rise of the absorption edge coupled with a very high excitonic absorption peak which makes this effect so attractive for optoelectronic modulators.

Fast and efficient optical intensity modulation has been demonstrated in transverse modulators, where light propagates perpendicularly to the well layers ( along the z axis allowing only TE polarization ) and in waveguide modulators where the light is guided parallel and along the MQW layers ( allowing for both TE and TM polarizations) [1,2].

The MQW waveguide utilizing structure A consists of an ( i ) guiding region of 15 pairs of 19 nm thick  $\text{Al}_{40}\text{Ga}_{60}\text{As}$  barriers with 6.5 nm thick GaAs wells, surrounded by a cladding layer of  $\text{Al}_{25}\text{Ga}_{75}\text{As}$ , on both sides. The 10 nm thick GaAs SQW is separated by 0.9  $\mu\text{m}$  from the center of the MQW. To form a p and p+ doped region on top of the MQW, metallic zinc of thickness 3000 Å was sputtered on, and the sample annealed for 5 minutes at 675 °C under flowing nitrogen gas. Ridge waveguides, 5 microns wide and 0.6 microns deep, were fabricated to confine the optical beam laterally. 4000 Å of  $\text{SiO}_2$  was then evaporated for electrical isolation between channels. After liftoff 2000 Å of gold was evaporated for p-type metalization. The substrate was then lapped down to a thickness of about 150 microns and n-type metalization was done by evaporating 2000 Å of Au-Ge. Figure 29 gives a vertical cross sectional schematic of the modulator. Figure 30 shows the current voltage characteristics (I-V) of the device and indicated a high quality device having a leakage current of 100 pA at -5Volts.

A 800 micron long modulator was fabricated by cleaving both ends, to give mirror like facets. Single mode behavior of this device was checked by doing near field measurements. An Argon ion laser pumped Ti-Sapphire was used as the light source. Figure 31 shows the near field intensity profiles for both the horizontal and vertical directions measured at a wavelength of 0.86 microns. The waveguide is single mode for both directions and the ridge made on top of the MQW region makes the device function as a strip loaded waveguide.

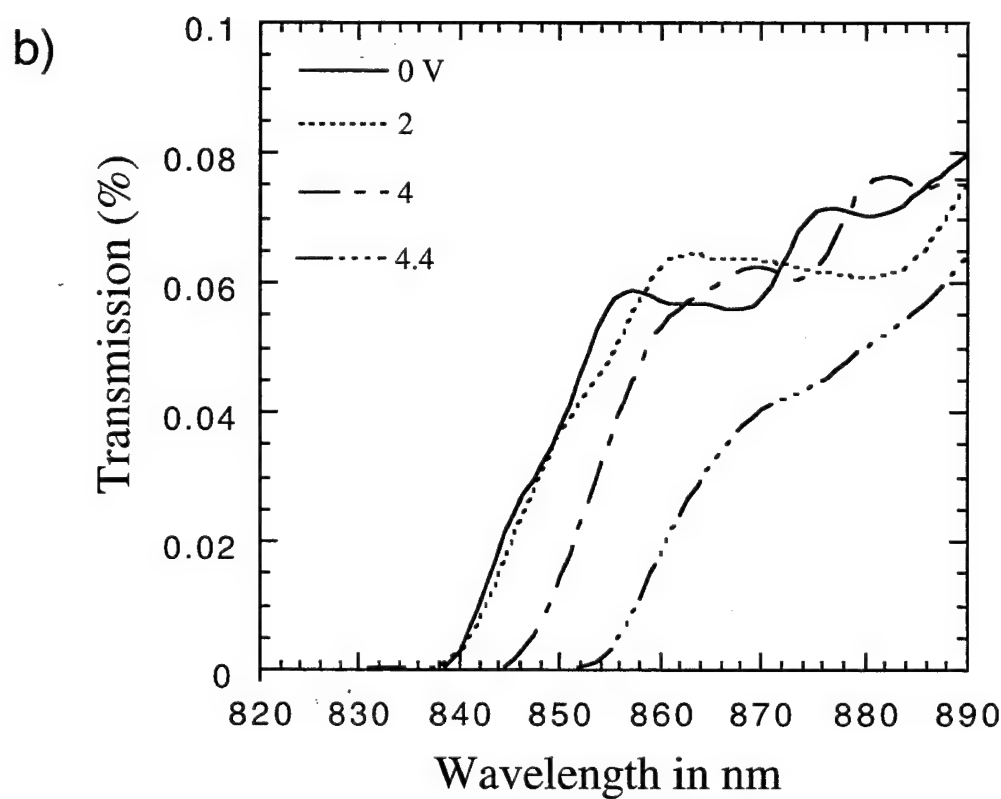
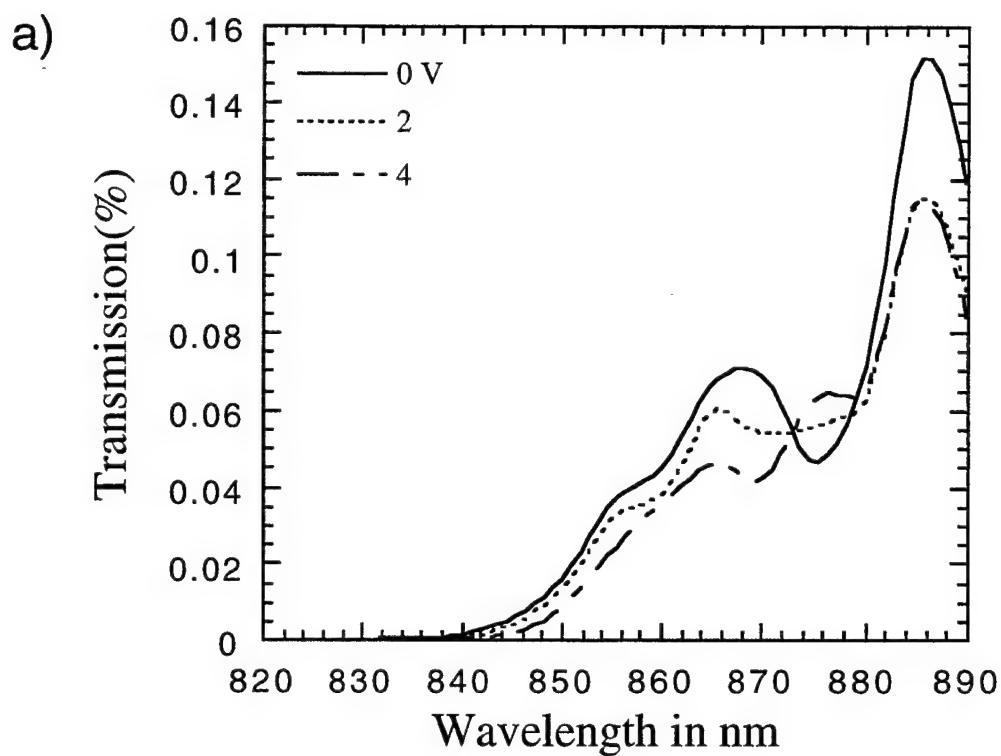


Figure 32: Variation of absorption spectra of MQW modulator with different bias voltages a) TE b) TM

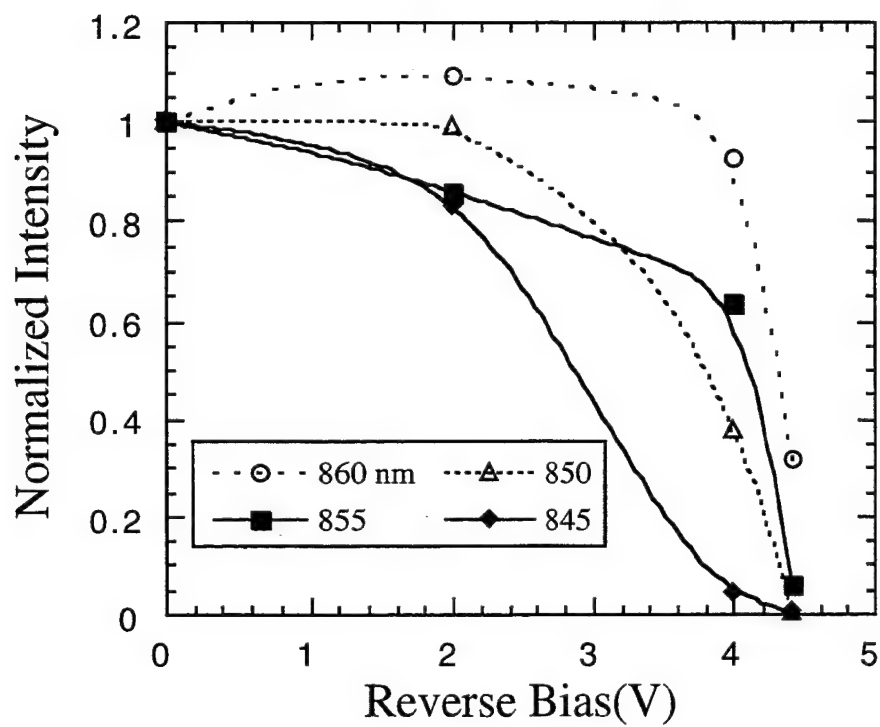
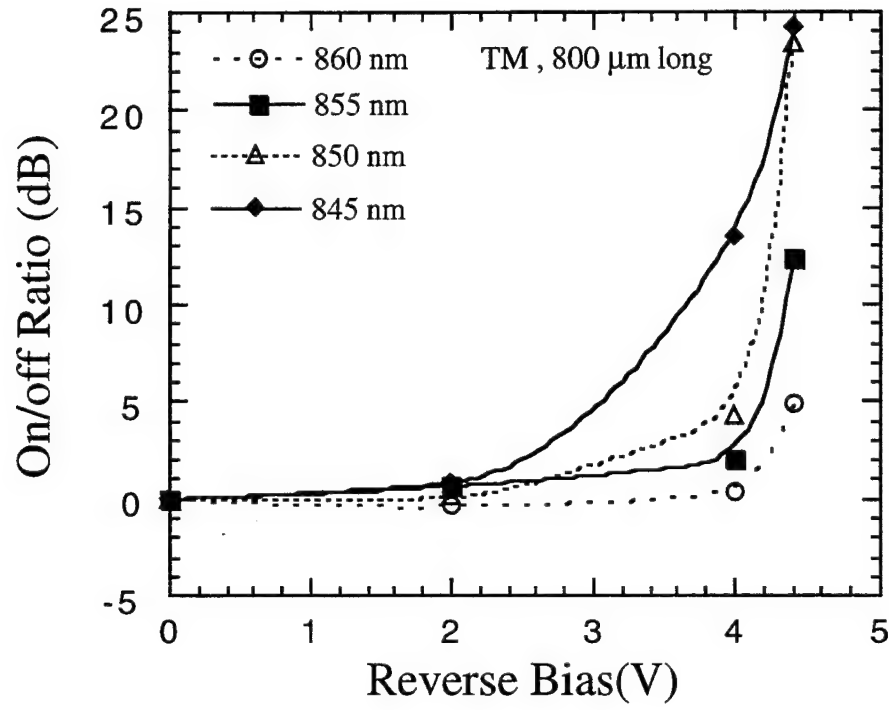


Figure 33: Intensity modulations at different wavelengths  
Intensity normalized to intensity at zero bias voltage



Variation in the on/off ratio of the intensity modulator at different wavelength

Figure 34

The absorption spectra measurements were done in a waveguide structure as a function of reverse bias voltage. The measured spectra for both TE and TM polarizations are shown in figures 32 a and b, respectively. The absorption does not change significantly for TE polarization, variations in the absorption edge and shape are observed. However, significant changes are observed for the TM case.

The output power variations were measured at wavelengths of 0.845, 0.850, 0.855 and 0.860 microns as a function of the reverse bias voltage across the modulator. Since it is an intensity modulation which is very sensitive to noise, a pin hole iris was used to filter extraneous light from guided light from the device. The measured intensity variations are presented in figure 33 for the case of TM polarized light, and the intensity is normalized by the intensity observed with zero bias voltage. Figure 34 is a representation of figure 33 with the intensity shown on a dB ( $-10\log(P_0/P_V)$ ) scale, where  $P_0$  and  $P_V$  are the power intensities without and with reverse bias voltage respectively. From the figure an on/off ratio of about 24 dB at wavelengths of 0.845 and 0.850 microns is obtained and is reasonably high compare to published values.

#### **Integration of tapered interconnect and modulator:**

The tapers were fabricated by gradually disordering sections of the MQW region in the the guided beam propagation direction permitting both the effective thickness of the MQW region as well as the refractive index, to be changed correspondingly. This results in the evolution of the mode from the SQW to the MQW region with propagation distance. For fabrication of the tapers, an  $\text{SiO}_x$  layer with thickness varying linearly from 0 to 300 nm was deposited by using a stepper motor controlled knife edge shadow mask during the  $\text{SiO}_x$  evaporation process. 300 nm of Zn was then evaporated and the sample annealed at 675 °C for 30 minutes for Zn impurity induced disordering or Fluorine, Oxygen or Nitrogen implanted at an energy of 125 keV and dosage of  $5 \times 10^{15}$  and the sample annealed. For modulation measurements, 7 micron wide and 0.3 micron deep

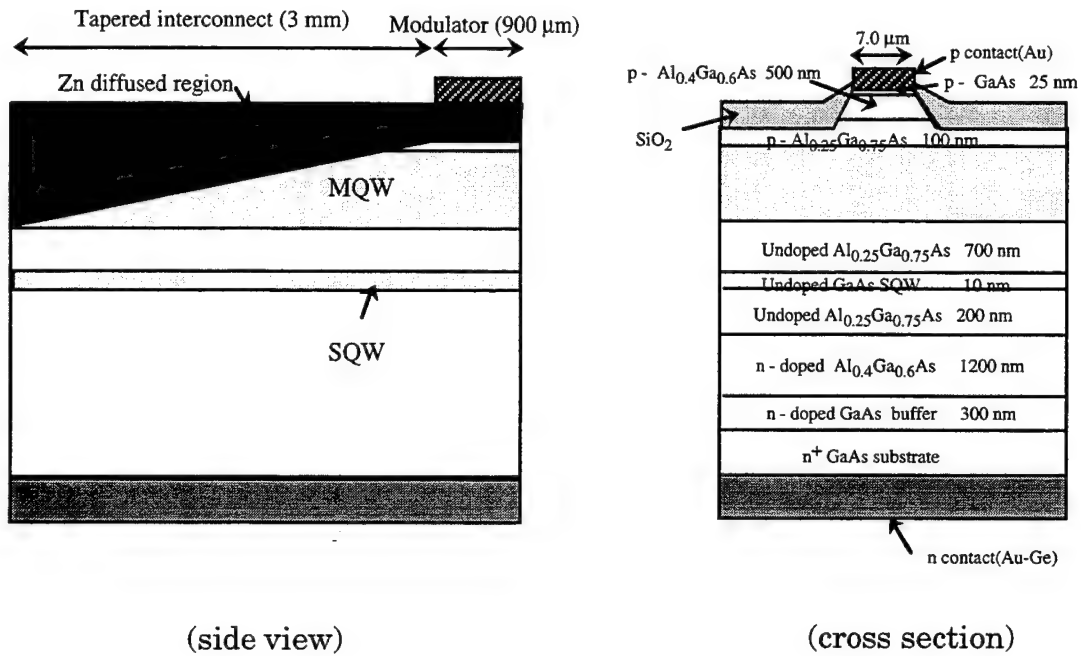


Figure 35: Schematic of the integrated structure of a tapered waveguide and electroabsorption modulator

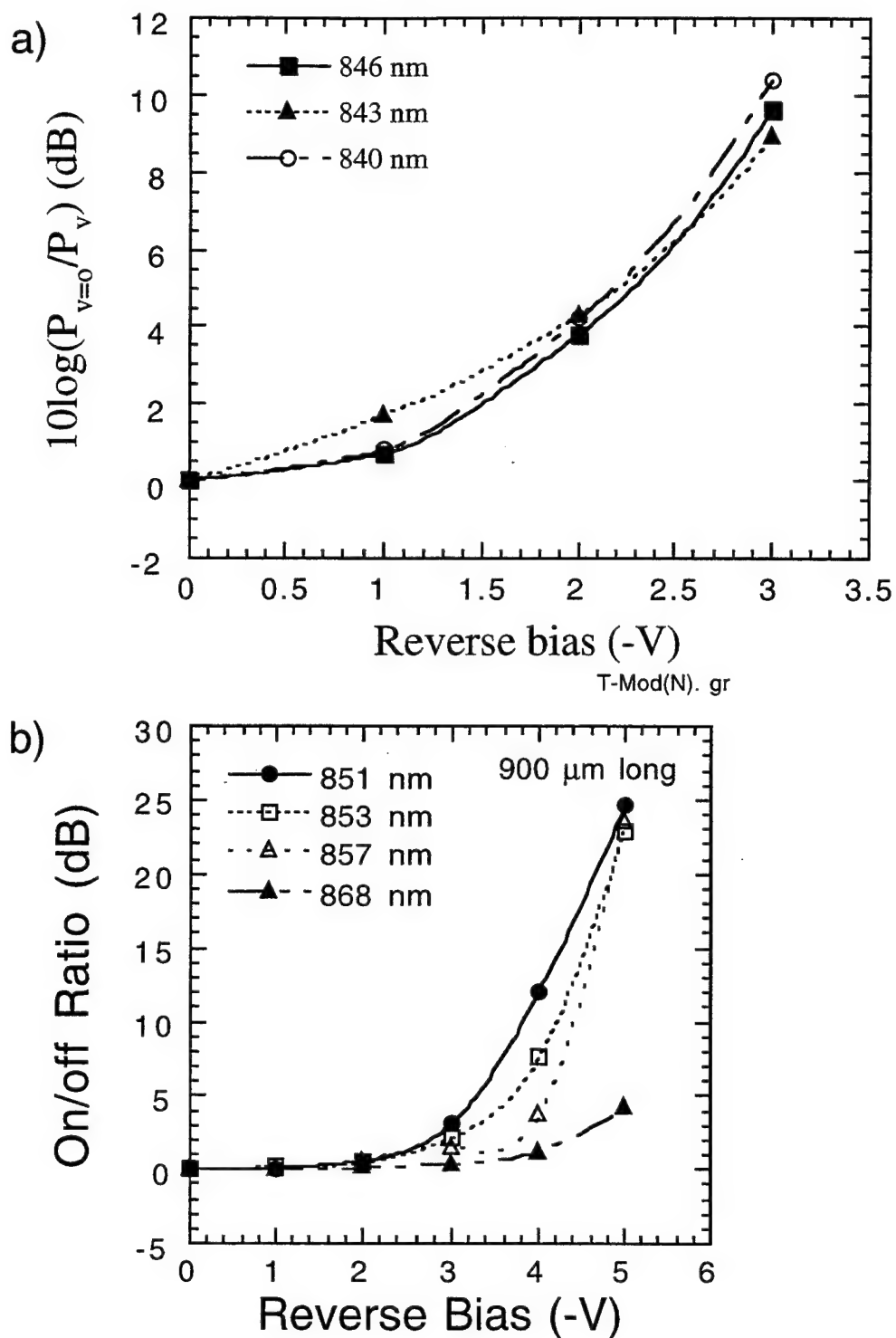


Figure 36: Intensity modulation as a function of reverse bias voltage for different wavelengths a) Zn diffused taper b) Nitrogen implanted taper.



ridges were fabricated to have lateral confinement of the beam. The p+ contact layer on the modulator section was formed by shallow Zn diffusion through the thick SiO<sub>x</sub> layer and passivation and metalization were performed sequentially. Figure 35 shows a lateral cross sectional view of the device.

Light from a Ti sapphire tunable laser was butt coupled into the most disordered end of the SQW section. Since the refractive index of the MQW changes according to the extent of disordering, index decreasing with increasing disordering, the fundamental normal mode of the structure evolves from the SQW to the MQW region, transferring energy from the SQW to the MQW region. To ensure that the beam is in the MQW layer before it enters the modulator section, the passive absorption profile at the end of the modulator was measured. From the fact that the beam is almost absorbed at 0.835 microns, it appears that the beam is completely transferred to the MQW layer in the modulator section. Electroabsorption measurements were performed utilizing a 900 micron long modulator section at wavelengths 0.84, 0.843 and 0.846 microns near the band edge.. Figure 36a represents the intensity modulation as a function of reverse bias voltage. A maximum on/off ratio of 10 dB was obtained at -3 V bias. Although the interaction length is long and the confinement factor  $\sim 0.2$ , the modulator efficiency is still not as high as that for the discrete MQW modulator. The previous measurements on the discrete modulator of the same structure gave a 23 dB on/off ratio at 4.4 V with less Zn diffusion and compares favorably with other published results. We attribute this poorer on/off ratio to difficulties associated in isolating the guided energy from scattered light in our near field measurements and the possibility of poor electrical isolation between the modulator and the passive tapered waveguide interconnect. Figure 36b represents the intensity modulation as a function of reverse bias voltage for the case of N implanted taper. The performance is about identical to that of a discrete device.

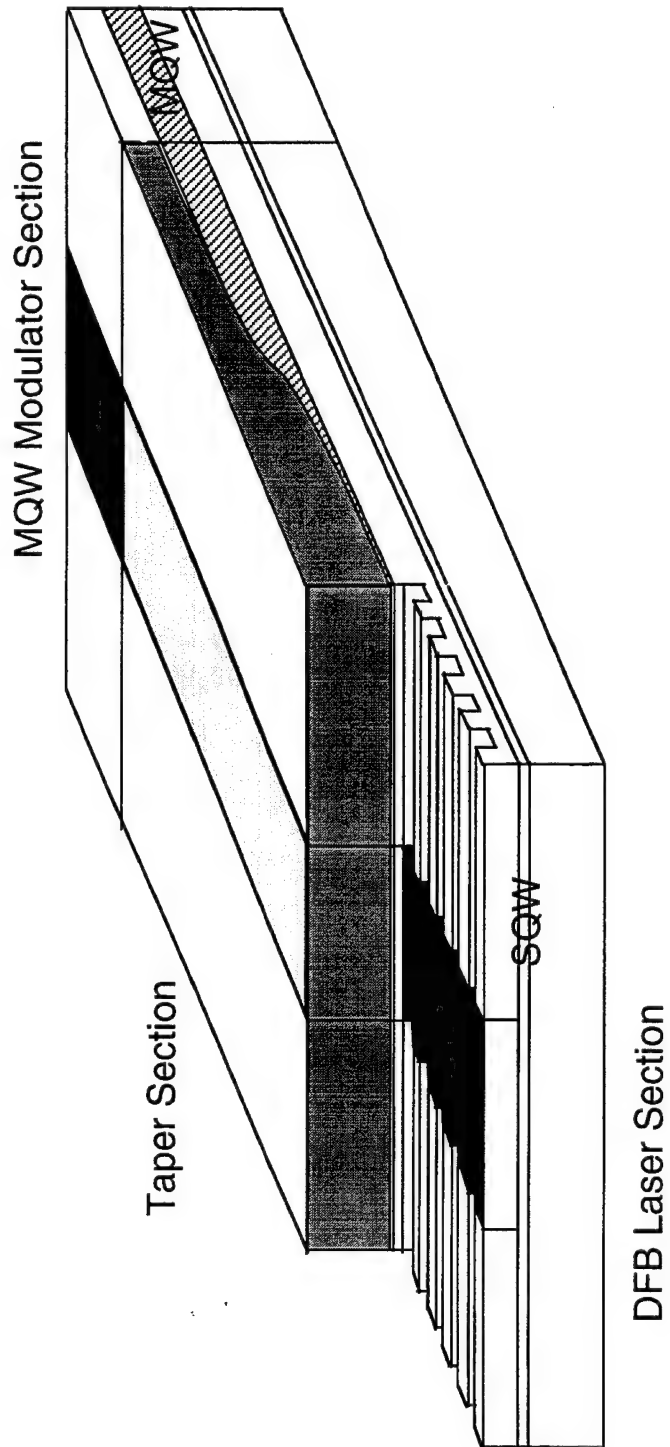


Figure 37: Scheme A for total Integration

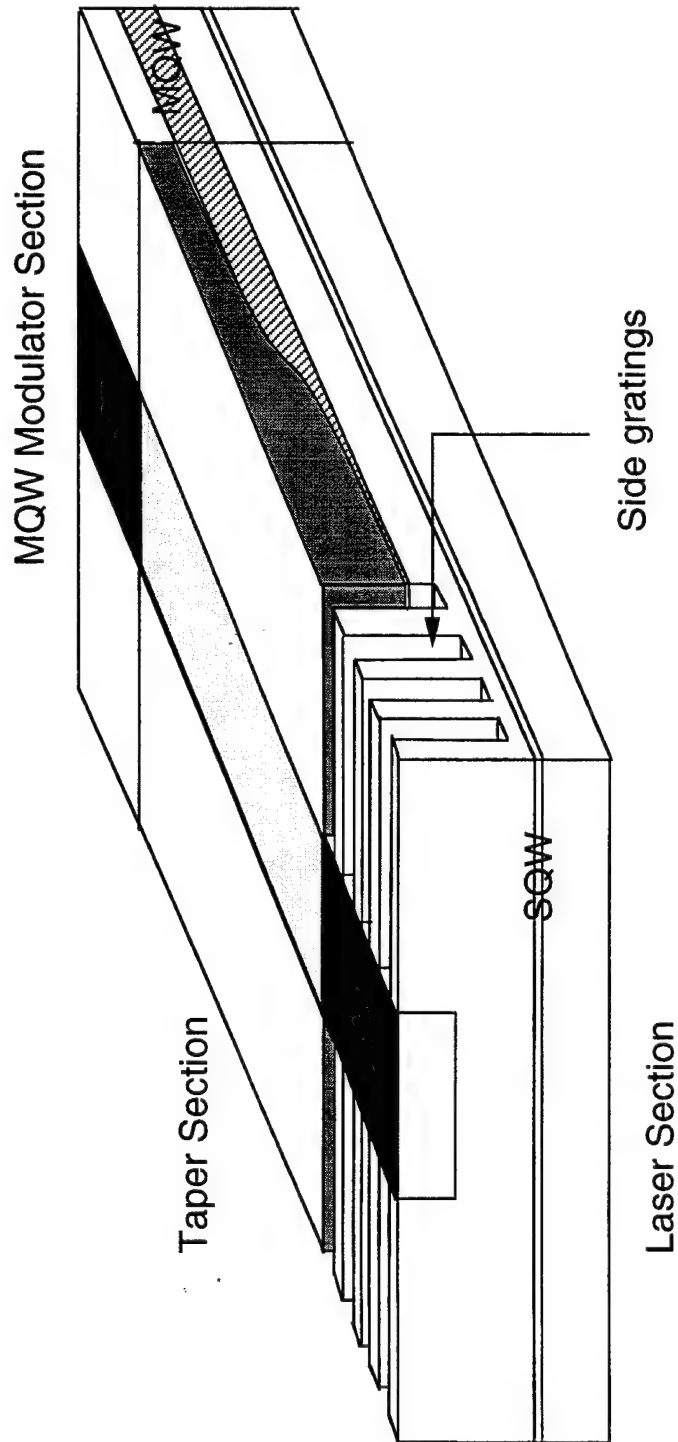


Figure 38: Scheme B for total Integration

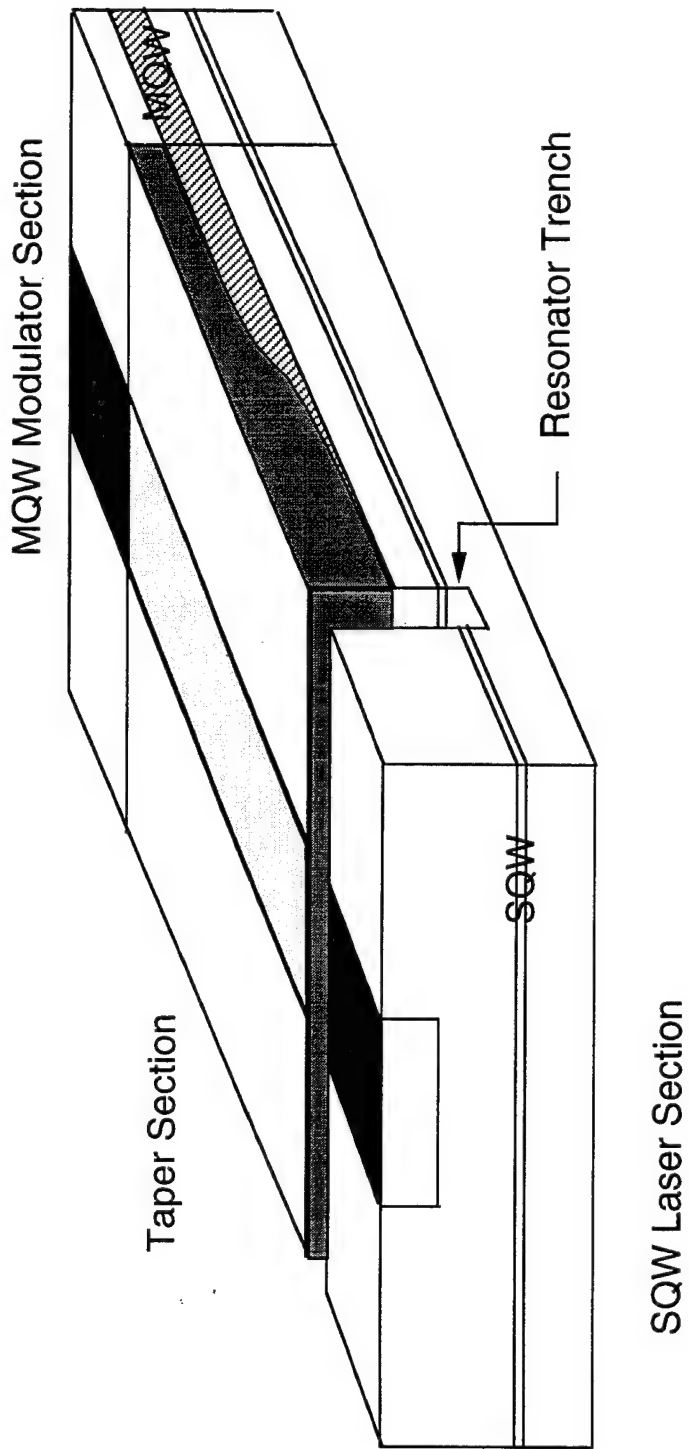


Figure 39: Scheme C for total Integration

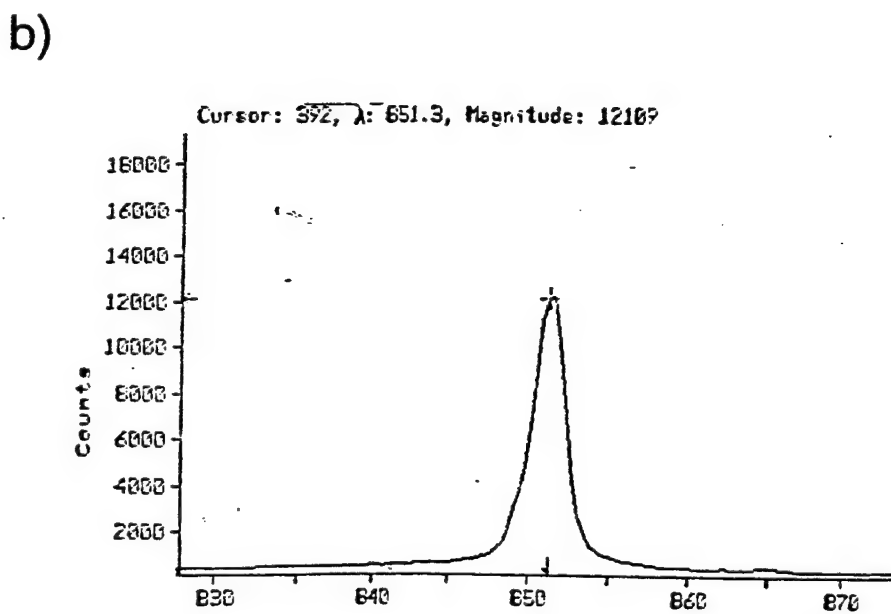
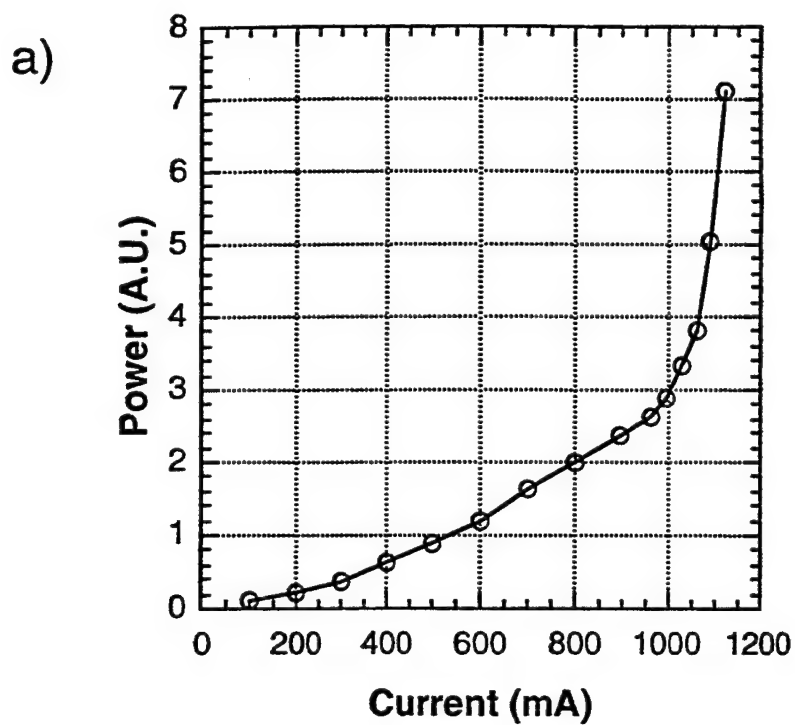


Figure 40: a) Power versus current for laser with etched trench.  
b) Spectrum of laser output

### **Integration of Laser-Taper and Modulator:**

As one end of the Fabry-Perot laser would be an integral part of the integrated Laser-Taper-Modulator chip, various schemes to provide adequate optical feedback for the laser to operate in this structure were pursued.

Figure 37 illustrates scheme a, which involves i) reactive ion etching/wet etching the top cladding in the laser section to a thickness of about 0.5 microns, ii) reactive ion etching a 3rd order grating defined by holographic photolithography, for the laser wavelength in the medium, and then metallizing the grating to give a shiny metal contact distributed feedback laser.

Laser action was observed in samples metallized after etching down the top cladding to a thickness of 0.5 microns. Threshold currents were similar to lasers with a thicker cladding. However, no laser action was observed in samples with the metallized gratings. This was attributed to poor metallization/contacts, due to oxidation of the grating surface and chirping of grating depth. This scheme was abandoned as it involved critical process technology, beyond the current technology level available in our laboratory.

Figure 38 illustrates scheme b, which involves reactive ion etching deep surface side gratings, defined by holographic photolithography, in the laser section. Such a scheme has indeed been reported with good lasing characteristics. However, this scheme was abandoned as it too involved critical process technology.

Figure 39 illustrates scheme c, which involves reactive ion etching a deep resonator trench of width  $W = (2n+1) \lambda / 4$ , between the laser section and the tapered interconnect. Laser action was observed in samples with etched resonator trenches, having width  $W = 5$  microns and depth  $d = 2$  microns. Figure 40 a,b shows the P-I curve and the spectrum of one such device.

The total integrated structure was fabricated as follows: Nitrogen ions of energy 125 kV, dosage  $1.5 \times 10^{15}/\text{cm}^2$  were implanted in the 3 mm wide taper section, through a

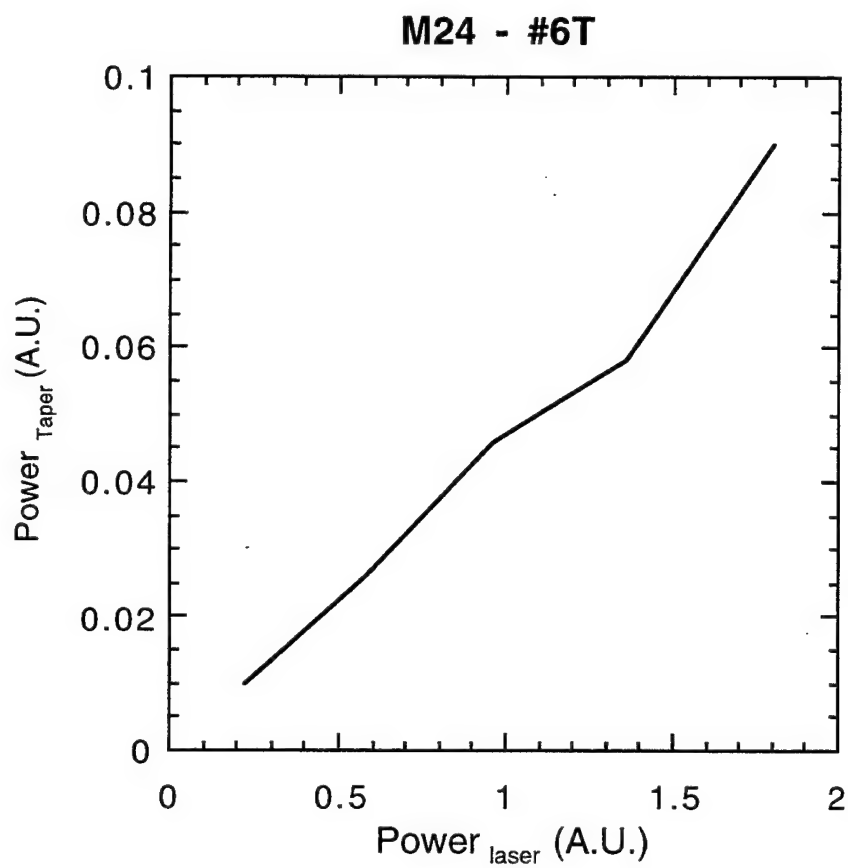


**Figure 41:** Power output from taper end versus power output from laser end

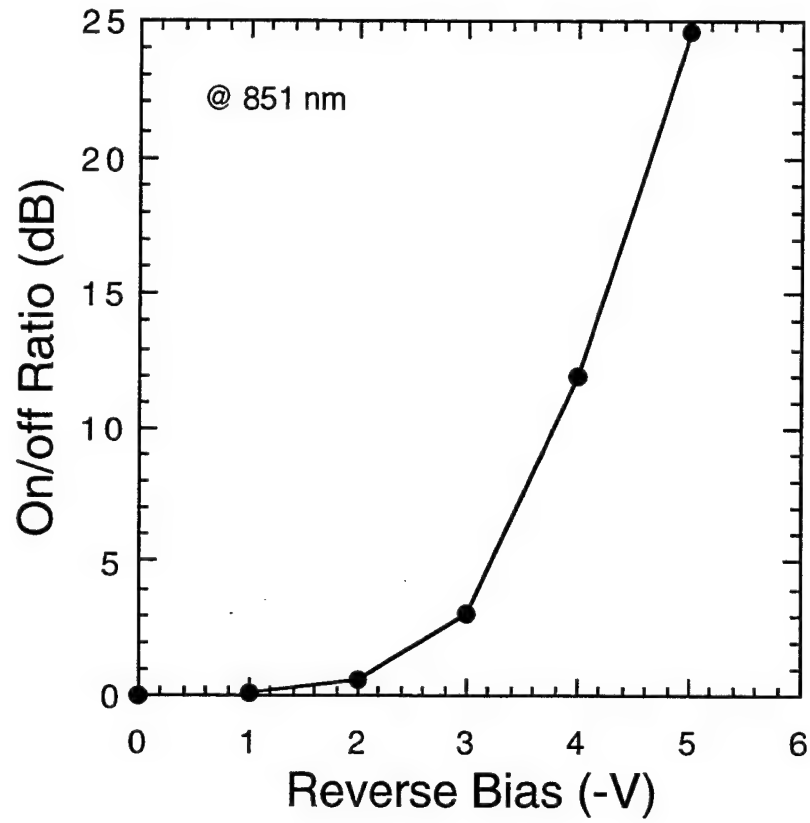


Figure 42: Modulator performance in integrated structure



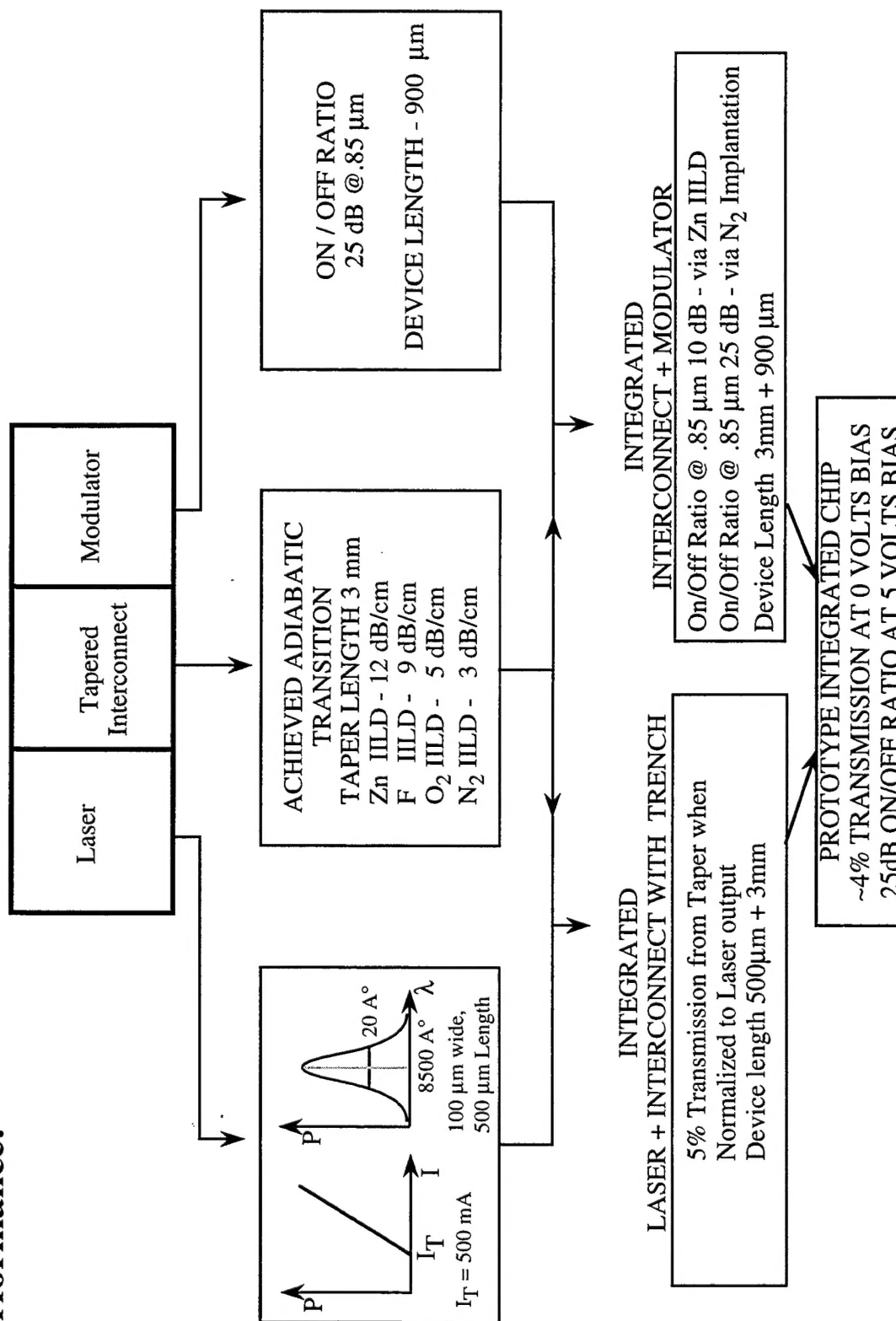
tapered  $\text{SiO}_x$  mask. Multiple Zn implants of energy 170 kV at angles of 0, 3 and 5 degrees to the sample normal and at a dosage of  $1.5 \times 10^{15}$  were done in the laser section. These samples were then capped with  $\text{SiO}_x$  and annealed at  $700^\circ\text{C}$  for 40 minutes to get rid of implant damage and disorder the MQW region. Two separate Zn diffusions were then done for the laser section and the modulator section. A 5 micron wide resonator trench was then selectively etched between the laser section and the tapered interconnect. These samples were then processed into waveguide type integrated devices as mentioned in the previous sections. Some samples were cleaved at the modulator-tapered interconnect interface.

Figure 41 shows the correspondance between power measured at the cleaved taper interconnect end with respect to the power measured from the cleaved end of the laser section in an integrated laser - taper interconnect.

Figure 42 shows the modulator performance as a function of reverse bias voltage at the laser wavelength.

# Summary

## Performance:



### **References:**

1. Y.Noda, M.Suzuki et.al., J.Lightwave Technology, Vol. LT-14, pp. 1445-1453, 1986.
2. F.K.Reinhart, Appl. Phys. Lett., Vol. 22, pp. 372-374, 1986.
3. G.E.Stillman, C.M.Wolfe et.al., Appl. Phys. Lett., Vol. 28, pp. 544-546, 1976.
4. N.K.Dutta and N.A.Olsson, Electron. Lett., Vol. 20, pp. 634-635, 1984
5. Y.Noda, M.Suzuki et.al., Electron. Lett., Vol. 21, pp. 1182-1183, 1985
6. J.C.Cambell et.al., Appl.Phys.Lett.,Vol. 32, pp. 471-473, 1978.
7. M.Suzuki et.al., Electron. Lett., Vol. 22, pp. 312-313, 1986.
8. M.Suzuki et.al., Trans.IECE Japan, Vol. E69pp. 395-398, 1986.
9. H.Ribot et.al., Appl.Phys.Lett., Vol. 55, pp. 672-674, 1989.
10. S.O'Brien et.al., Appl.Phys.Letts., Vol. 58, pp. 1363-1365, 1991
11. W.X.Zou., Appl.Phys. Letts., Vol. 62, pp. 556-558, 1993.
12. S.Tarucha and H.Okamoto., Appl. Phys.Lett., Vol. 48, pp. 1-3, 1986.
13. R.Thornton, W.Mosby and T.Paoli, J. Lightwave Technology, Vol. 6,pp.786-792, 1988.
14. W.D.Laidig et.al., Appl. Phys.Lett., Vol 38, pp776-778,1981.
15. E.H.Li et.al., Appl.Phys. Letts.,Vol 62,pp 550-552,1993.
16. M.E.Maney, J.Appl.Phys., Vol72, pp 5729-5734,1992.
17. M.A.Afromowitz, Solid State Comm., Vol 15,pp 59-63,1974.
18. C.P.Hussell et.al., Appl.Optics, Vol 29, pp 4105-4110, 1990.
19. H.S.Kim et.al., IEEE Photon.Technol.Lett., Vol 5, pp 1049-1052, 1993.
20. D.Marcuse, Bell Sys. Tech. J., Vol 49, pp 273-290,1970.
21. A.F.Milton and W.K.Burns, Appl. Optics, Vol 14, pp 1207-1212, 1975.
22. R.N.Thurston et al., IEEE J.Quantum Electron., Vol QE-23,pp 1245-1255, 1987.
23. S.K.Han et al., Tech. Dig. IPR.Topical Meeting, San Francisco, CA, 1994, Paper ThF 29.

**List of Publications::**

- 1)" Tailoring of Electron and Hole Energies in Strained GaAsP/AlGaAs Quantum Wells using Fluorine Impurity Induced Layer Disordering ", U.Das, S.Davis, R.V.Ramaswamy and F.A.Stevie, Appl. Phys. Lett., Vol 60, pp 210, 1992.
- 2)" Tapered waveguide interconnect using Zn diffusion induced layer disordering of quantum wells ", S.Sinha, R.V.Ramaswamy, X.Cao and U.Das, LEOS Summer Topical Meeting on Integrated Optoelectronics, Paper THC3, Santa Barbara, CA. Aug. 5 1992.
- 3) " Efficient Phase Modulation in InGaAlAs/InP waveguides ", S.K.Han, R.V.Ramaswamy, IEEE/LEOS'92, Paper OTA3.3, Boston, MA, Nov. 1992.
- 4)" Efficient Electro-Optic Modulator in InGaAlAs/InP Optical waveguides ", S.K.Han, R.V.Ramaswamy, W.Q.Li and P.K.Bhattacharya, IEEE Photonics Tech. Lett., Vol. 5, No. 1, pp. 46, 1993.
- 5)"Fluorine implantation induced tapered waveguide interconnect",S.K.Han, M.Subramanian, S.Sinha and R.V.Ramaswamy, Appl. Phys. Lett., Vol. 63, pp.2735, 1993.
- 6)"An MQW-SQW tapered waveguide transition ", H.S.Kim, S.Sinha and R.V.Ramaswamy, IEEE Photonics Tech. Lett., Vol. 5, pp.1049, 1993.
- 7)" Effect of Zinc impurity induced disordering on the refractive index of GaAs/AlGaAs multi quantum wells", S.K.Han, S.Sinha and R.V.Ramaswamy, Appl. Phys. Lett., Feb 7, 1994.
- 8)" Integration of a tapered waveguide with an electroabsorption multi quantum well modulator", S.K.Han, S.Sinha and R.V.Ramaswamy, IPR '94.
- 9)" Zinc diffusion studies through an SiO<sub>x</sub> barrier into GaAs/AlGaAs structures", S.Muthu, S.Sinha and R.V.Ramaswamy, LEOS Topical Conference, 1994.
- 10)" Tapered waveguide interconnects: experiments and analysis", H.S.Kim, S.K.Han, S.Sinha and R.V.Ramaswamy, to be communicated to Journal of Quantum Electronics.
- 11) "Implant Energy dependence of Fluorine Impurity Induced Disordering of GaAsP/AlGaAs quantum wells", U. Das, S.Sinha, R.V.Ramaswamy and F.A.Stevie, to be communicated to Applied Physics Letters.
- 12) "Integration of low loss tapered waveguide with an absorption edge MQW modulator", S.Sinha, S.K.Han and R.V.Ramaswamy, Electronics Letters, To be communicated.
- 13) "A novel scheme for Zinc diffusion into GaAs and GaAs/AlGaAs structures", S.Sinha, R.V.Ramaswamy and B.Pathengay, Appl.Phys. Letts., To be communicated